Monthly Notices of the ROYAL ASTRONOMICAL SOCIETY

MNRAS **00,** 1–22 (2025) https://doi.org/10.1093/mnras/staf1933
Advance Access publication 2025 November 6

Probing the accretion geometry of black hole X-ray binaries: a multimission spectro-polarimetric and timing study

Seshadri Majumder [1★] Ankur Kushwaha [2] Swapnil Singh [2] Kiran M. Jayasurya [2] Santabrata Das [1★] and Anuj Nandi [2★]

[1]*Department of Physics, Indian Institute of Technology Guwahati, Guwahati 781039, India*
[2]*Space Astronomy Group, ISITE Campus, U. R. Rao Satellite Centre, Outer Ring Road, Marathahalli, Bangalore 560037, India*

Accepted 2025 November 1. Received 2025 November 1; in original form 2025 May 8

ABSTRACT

We present a comprehensive spectro-polarimetric and timing analysis of 12 black hole X-ray binaries, namely Cyg X−1, 4U 1630−47, Cyg X−3, LMC X−1, 4U 1957+115, LMC X−3, *Swift* J1727.8−1613, GX 339−4, *Swift* J151857.0−572147, IGR J17091−3624, MAXI J1744−294, and GRS 1915+105, using quasi-simultaneous observations from *IXPE* (Imaging X-ray Polarimetry Explore*r)*, *NICER* (Neutron star Interior Composition Explorer), *NuSTAR* (Nuclear Spectroscopic Telescope Array), and *AstroSat*. Timing analyses reveal type-B and type-C quasi-periodic oscillations across different spectral states, often associated with episodic radio ejections. Broad-band (0.7–60 keV) spectral modelling, employing disc, Comptonization, and reflection components, reveals degeneracies in constraining disc–corona geometries. Polarimetric measurements in 2–8 keV band detect significant polarization degrees (PDs) ranging from 3 per cent–20.6 per cent (1.2 per cent–21.4 per cent) in harder (softer) states, with moderate to strong energy dependence, except for LMC X−1, *Swift* J151857.0–572147, and MAXI J1744−294, where no significant polarization is detected. We report polarization detections of Cyg X−3 (PD $\sim$ 21.4 per cent, soft intermediate state), LMC X−3 (PD $\sim$ 2.4 per cent, high-soft state), and IGR J17091–3624 (PD $\sim$ 9 per cent, low-hard state) using recent *IXPE* observations. A positive correlation is found between PD and Comptonized photon fraction ($cov_{\rm frac}$), while an anticorrelation is observed with disc-to-Comptonized flux ratio ($F_{\rm ratio}$) across spectral states. Combined timing, spectral, and polarimetric results, together with constraints from radio jet observations, suggest a radially extended corona within a truncated disc for Cyg X−1, *Swift* J1727.8–1613, IGR J17091–3624, and GX 339–4, whereas the disc–corona geometry remains poorly constrained for 4U 1957+115, LMC X−3, and 4U 1630–47. We discuss the implications of these findings for understanding accretion geometries and highlight prospects for future X-ray polarimetric studies.

Key words: accretion, accretion disc – black hole physics – polarization – radiation mechanisms: general – stars: individual – X-rays: binaries.

1 INTRODUCTION

Black hole X-ray binaries (BH-XRBs) are believed to be the ideal candidates for understanding the physical processes that govern the radiation mechanism around the compact objects. BH-XRBs often exhibit distinct spectral states over time-scales ranging from days to months, strongly associated with the underlying accretion dynamics of the system (E. H. Morgan, R. A. Remillard & J. Greiner 1997; C. Done & P. T. Zycki 1999; S. K. Chakrabarti & S. G. Manickam 2000; J. Homan et al. 2001; T. Belloni et al. 2005; R. A. Remillard & J. E. McClintock 2006; A. Nandi et al. 2012, 2024; N. Iyer, A. Nandi & S. Mandal 2015; H. Sreehari et al. 2019b; B. E. Baby et al. 2020; M. P. Athulya et al. 2022; S. Majumder et al. 2022; G. Prabhakar et al. 2023; P. Majumder, B. G. Dutta & A. Nandi 2025, and references therein). Empirically, the high-soft state (HSS) is characterized by the multitemperature blackbody emission that is likely to emerge from an optically thick and geometrically thin accretion disc (N. I. Shakura & R. A. Sunyaev 1973). In contrast, the canonical low-hard state (LHS), represented by a power-law profile with high energy cut-off, is found to be dominated by the hard emission produced from the Compton upscattering of disc photons into the 'hot' electron cloud (equivalently X-ray corona). Moreover, depending on the relative contributions from the disc and coronal components, hard/soft intermediate states (HIMS/SIMS) are observed.

Needless to mention that the possible geometry of the Comptonizing corona in BH-XRBs remains an unsettled issue to date. Several alternative scenarios featuring the models of the sandwich corona (F. Haardt & L. Maraschi 1993; B. E. Stern et al. 1995), radially elongated corona at the truncated inner accretion disc (D. M. Eardley, A. P. Lightman & S. L. Shapiro 1975; S. Chakrabarti & L. G. Titarchuk 1995; J. Poutanen, J. H. Krolik & F. Ryde 1997; N.

★ E-mail: smajumder@iitg.ac.in (SM); sbdas@iitg.ac.in (SD); anuj@ursc.gov.in (AN)

Iyer et al. 2015), and vertically extended corona as the base of the jet (S. Miyamoto & S. Kitamoto 1991; S. Markoff, M. A. Nowak & J. Wilms 2005; M. Méndez et al. 2022; Y. Zhang et al. 2023) have been proposed over the years. However, the overall geometry of the disc–corona–jet remains elusive mostly due to the model degeneracies that complicate the interpretation of the observational data.

Notably, the temporal properties of BH-XRBs show rapid X-ray variability over different time-scales. This variability is usually observed in the power density spectrum (PDS) and is closely correlated to the spectral states. In particular, transient phenomena like strong and stable low-frequency quasi-periodic oscillations (LFQPOs) on a wide range of frequencies distinguish the spectral states and act as the precursor of the state transitions in BH-XRBs (R. A. Remillard & J. E. McClintock 2006; C. Done, M. Gierliński & A. Kubota 2007; A. Nandi et al. 2012; N. Iyer et al. 2015). For example, the LHS and HIMS are characterized by the appearance of strong, coherent, variable peaked type-C LFQPO of frequency ∼0.1–15 Hz superposed on a flat-top noise (FTN) component in the PDS (R. A. Remillard & J. E. McClintock 2006; A. Nandi et al. 2012, and references therein). The origin of these type-C QPOs is often explained through various mechanisms, including oscillations of radiative shock waves within the accretion disc (D. Molteni, H. Sponholz & S. K. Chakrabarti 1996; S. K. Chakrabarti et al. 2008; S. Das et al. 2014), relativistic Lense–Thirring precession of the inner hot flow or the truncated disc (L. Stella & M. Vietri 1998; A. Ingram, C. Done & P. C. Fragile 2009), precession of small-scale jets (X. Ma et al. 2021) and outward drift of the truncated inner disc radius enveloped by the corona (K. Karpouzas et al. 2020; C. Bellavita et al. 2022, 2025). The wide array of interpretations introduces a degeneracy among different disc–corona–jet configurations used in explaining QPO phenomena (see A. R. Ingram & S. E. Motta 2019 for a review).

On the other hand, relatively weak type-B/type-A QPOs appear at a narrow frequency range of around ∼6–8 Hz (P. Casella, T. Belloni & L. Stella 2005) during the SIMS. In this state, FTN is absent, and the PDS continuum shows weak red noise characterized by a simple power law in PDS continuum. These type-B/type-A QPOs are often found to be closely connected with the radio ejections generally observed in the SIMS (P. Soleri, T. Belloni & P. Casella 2008; R. P. Fender, J. Homan & T. M. Belloni 2009; J. Homan et al. 2020; N. D. Kylafis, P. Reig & I. Papadakis 2020; F. García et al. 2021; H. X. Liu et al. 2022; Y. Zhang et al. 2023). Usually, soft states are characterized by less variability in the PDS without the detection of QPO like features (T. Belloni et al. 1999, 2005; A. Nandi et al. 2012; D. Radhika & A. Nandi 2014; D. Radhika et al. 2016).

Furthermore, X-ray polarimetric study is also considered a powerful diagnostic tool to infer the accretion geometry of the BH-XRBs. The recent launch of *IXPE* (M. C. Weisskopf et al. 2022), a polarimetric mission sensitive to low-energy (2–8 keV) X-rays, enables the opportunity to investigate in-depth polarimetric properties of BH-XRBs. So far, *IXPE* has observed 12 BH-XRBs, namely Cyg X−1, 4U 1630−47, Cyg X−3, LMC X−3, LMC X−1, 4U 1957+115, *Swift* J1727.8−1613, *Swift* J151857.0−572147, GX 339−4, IGR J17091−3624, MAXI J1744−294, and GRS 1915+105 with significant polarized emission detected in eight sources (see also M. Dovčiak et al. 2024).

Despite the significant advancements in X-ray polarimetry, interpreting the observed polarization degree (PD) and polarization angle (PA) within the framework of theoretical models remains a formidable challenge. The classical work by Chandrasekhar (S. Chandrasekhar 1960) on semi-infinite electron scattering predicts a low PD of ∼2 per cent from the accretion disc of highly inclined systems. However, 4U 1630−47 shows a remarkably higher PD of around 8.3 per cent in its disc-dominated thermal state, deviating substantially from these theoretical expectations (A. Kushwaha et al. 2023; A. Ratheesh et al. 2024). Similarly, soft state observations of Cyg X−1 show polarization perpendicular to the disc plane, whereas theoretical models predict it to be parallel. This possibly indicates a rapidly rotating black hole in Cyg X−1, responsible for the returning radiation effects seen in the spectro-polarimetric data (H. Krawczynski et al. 2024; J. F. Steiner et al. 2024). Furthermore, PDs of about 4 per cent have been observed in the LHS of Cyg X−1 and *Swift* J1727.8−1613 (H. Krawczynski et al. 2022; A. Ingram et al. 2024), whereas existing models predict only ∼1 per cent PD from a wedge-shaped corona in such low-inclined systems (H. Krawczynski et al. 2022). To reconcile this discrepancy, J. Poutanen, A. Veledina & A. M. Beloborodov (2023) invoked the model of A. M. Beloborodov (1998) of an outflowing corona with mildly relativistic motion to explain the high PD levels. It is worth mentioning that the recent detection of ∼9 per cent PD in the LHS of IGR J17091−3624 (M. Ewing et al. 2025) further indicates the limitations of current theoretical frameworks and highlights the need for more comprehensive models of X-ray polarization.

Moreover, in certain cases, the spectro-temporal findings of BH-XRBs appear to be contradictory with interpretations derived from X-ray polarimetry. For instance, in *Swift* J1727.8−1613, the evolution of type-C QPOs suggests the presence of a jet-like corona aligned perpendicular to the disc plane (J. Liao et al. 2024). In contrast, simultaneous polarimetric observations of the same source indicate a radially extended corona resided at the equatorial plane of the disc (A. Veledina et al. 2023; A. Ingram et al. 2024). Therefore, it is evident that the polarimetric findings offer challenges to the existing X-ray spectro-temporal models, indicating that a deeper understanding of the accretion dynamics and disc–corona–jet geometry in BH-XRBs is yet to be unveiled.

Being motivated by this, we carry out in-depth timing and spectro-polarimetric analyses of 11 BH-XRBs using quasi-simultaneous archival observations from *IXPE*, *NICER*, *NuSTAR,* and *AstroSat*, covering a broad energy range of 0.5–100 keV. We conduct a comprehensive spectro-temporal study of these sources using *NICER*, *NuSTAR,* and *AstroSat* data and confirm the presence of distinct spectral states of the BH-XRBs during the observational campaigns. Further, we deduce the polarization properties of the sources using *IXPE* data in the 2–8 keV energy range, followed by a detailed spectro-polarimetric correlation study. Notably, the timing and spectro-polarimetric results serve as powerful diagnostics offering deeper insights into the complex accretion dynamics and geometry of BH-XRBs under consideration.

The paper is organized as follows. In Sections 2 and 3, we present the source selection with observation details and the data reduction procedures, respectively. The analysis and results of the timing and spectro-polarimetric study are presented in Section 4. Finally, we discuss the results and present conclusions in Sections 5 and 6, respectively.

2 SOURCE SELECTION AND OBSERVATIONS

In this work, we analyse all the *IXPE* (M. C. Weisskopf et al. 2022) observations of BH-XRBs conducted so far along with simultaneous/quasi-simultaneous *NICER*, *NuSTAR,* and *AstroSat* observations depending on data availability. As of now, *IXPE* observed twelve BH-XRBs during its first three and a half years of operational period. The *IXPE*, *NICER*, and *NuSTAR* observations

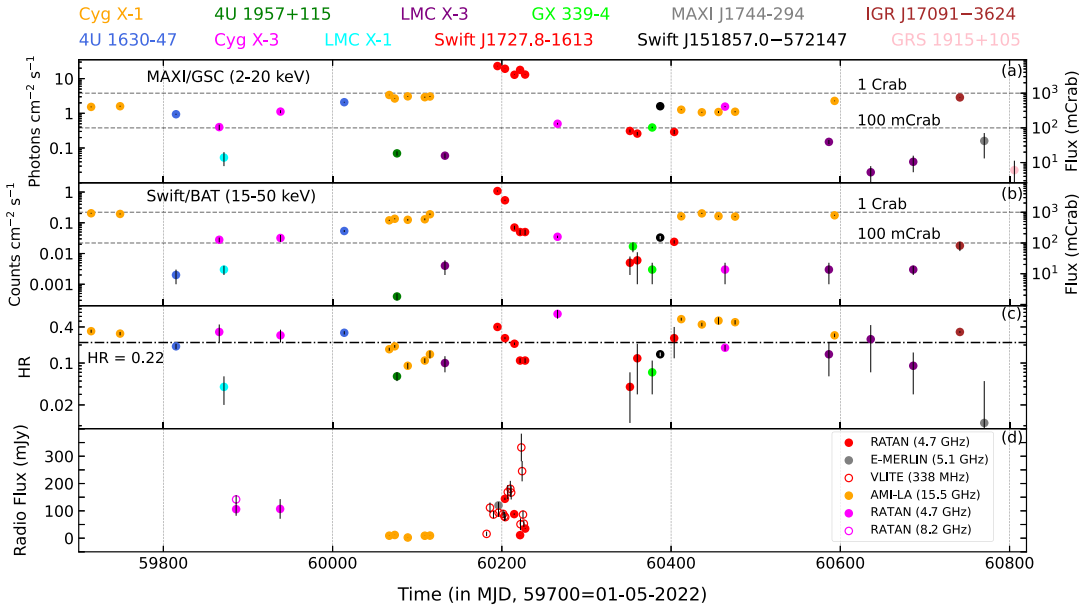

Figure 1. Long-term X-ray monitoring of the sources with *MAXI*/GSC (2–20 keV), *Swift*/BAT (15–50 keV), and the corresponding hardness ratio obtained with *MAXI*/GSC are presented in panels (a), (b), and (c), respectively. Each data point for a given source represents averaged out respective quantity over the exposure of corresponding *IXPE* observation. In panel (d), the variation of radio flux is shown from the quasi-simultaneous radio observations available from various facilities. The 1σ errorbars of the respective quantities are small and remain within the markers for most of the cases. For a given source, the data points plotted with MJD, correspond to the respective epochs as mentioned in Table 1.

used in this work are publicly available in the HEASARC[1] data base and the *AstroSat* data are archived at the ISSDC[2] website. The quasi-simultaneous multimission observations of the sources are separated by at most 3 d from the *IXPE* epoch except LMC X−1 for which the *NuSTAR* observation lies 4 d after the *IXPE* observation. The sources exhibiting marginal spectro-temporal variability between observations from different missions offer an opportunity for a combined multimission study. We mention that *IXPE* monitoring of GRS 1915+105 was carried out on 2025 May 10 for about ∼142 ks. However, the source remained below the detection level with *IXPE*, showing a *MAXI*/GSC (Monitor of All-sky X-ray Image/Gas Slit Camera) flux of ∼6 mCrab (see Fig. 1). Therefore, GRS 1915+105 is excluded from the detailed analyses in the following sections. All the observations analysed in this study are tabulated in Table 1. A brief overview of each of the sources under consideration are presented below.

• **Cyg X−1:** This is the first galactic BH-XRB discovered in 1971 (B. L. Webster & P. Murdin 1972), continues to be one of the most extensively studied celestial objects. Recent measurements reveal that it hosts a black hole with a mass of 21.2 ± 2.2 M$_\odot$, located at a distance of 2.2 ± 0.2 kpc, with a supergiant O-type star as its binary companion (J. C. A. Miller-Jones et al. 2021). Meanwhile, numerous studies confirm the presence of a maximally rotating black hole having spin greater than 0.99 at the centre core of the binary system (J. A. Tomsick et al. 2013; L. Gou et al. 2014; A. Kushwaha, V. K. Agrawal & A. Nandi 2021; X. Zhao et al. 2021). Cyg X−1 has remained persistently bright, mostly in the LHS, though it has transitioned to the HSS through short-lived intermediate states over the past few decades (A. Kushwaha et al. 2021). Interestingly, significant polarized emission is detected in both LHS and HSS of the source (H. Krawczynski et al. 2022; A. Jana & H.-K. Chang 2024; J. F. Steiner et al. 2024).

[1]https://heasarc.gsfc.nasa.gov/db-perl/W3Browse/w3browse.pl
[2]https://webapps.issdc.gov.in/astro_archive/archive/Home.jsp

• **4U 1630−47:** This is a recurrent X-ray transient discovered by *Uhuru* (C. Jones et al. 1976). Since discovery, the source has exhibited more than 20 quasi-period outbursts (B. E. Baby et al. 2020; K. Chatterjee et al. 2022) typically in every 600–700 d (A. N. Parmar, L. Angelini & N. E. White 1995). Several efforts relying on indirect measurements constrained its mass as 10 ± 0.1 M$_\odot$ (E. Seifina, L. Titarchuk & N. Shaposhnikov 2014), distance as 10–11 kpc (E. Seifina et al. 2014; E. Kalemci, T. J. Maccarone & J. A. Tomsick 2018), and high inclination i∼60°–70° (J. A. Tomsick, I. Lapshov & P. Kaaret 1998; E. Seifina et al. 2014). Spectral modelling (M. Pahari et al. 2018) and spectro-polarimetric fitting in the HSS confirm its spin as ∼0.92 (A. Kushwaha et al. 2023). Notably, 4U 1630−47 is the second source observed by *IXPE* for which a remarkably high polarization degree (∼6–8 per cent) has been detected in both thermal and steep power-law (SPL) states (A. Kushwaha et al. 2023; N. Rodriguez Cavero et al. 2023; D. Rawat, A. Garg & M. Méndez 2023b; A. Ratheesh et al. 2024).

• **Cyg X−3:** It was discovered over five decades ago (R. Giacconi et al. 1967) and is a high-mass X-ray binary system hosting a compact object accreting from a Wolf–Rayet donor star (M. H. Kerkwijk et al. 1992). Despite extensive studies over the years, the nature of the compact object remains uncertain. Recent polarization measurements suggest that it could be a concealed Galactic ultraluminous X-ray source (ULX) surpassing the Eddington limit due to anisotropic emissions (A. Veledina et al. 2024a). Recent measurements from *VLBA* (Very Long Baseline Array) observations have precisely constrained the distance of the source as $9.67^{+0.53}_{-0.48}$ kpc (M. J. Reid & J. C. A. Miller-Jones 2023).

• **LMC X−1:** This is the first discovered extragalactic persistent BH-XRB located in the Large Magellanic Cloud (LMC) (H. Mark et al. 1969) at a well-constrained distance of ∼48.1 kpc (G. Pietrzyński et al. 2013). Dynamical measurements have determined the black hole's mass to be 10.9 ± 1.4 M$_\odot$ with a moderate inclination of $36.4^\circ \pm 1.9^\circ$ (J. A. Orosz et al. 2009). The measurements using the continuum fitting method in the thermally

Table 1. Details of the multimission observations of the selected sources over different epochs. In the table, blue shades represent the epochs for which quasi-simultaneous *IXPE*, *NICER*, and *NuSTAR* observations are available. The grey shades denote the quasi-simultaneous observations with *IXPE* and *NICER* only. The magenta coloured shade indicates the epoch for which only quasi-simultaneous *IXPE* and *NuSTAR* observations are available. The orange coloured shade denotes the available *AstroSat* observations close to the *IXPE* epochs. See the text for details.

Source	Epoch	Instrument	Obs. ID	Start Date	MJD Start	Exposure (ks)	Mean Rate (cts/s)	*MAXI/GSC* Flux (mCrab) (2 − 20 keV)	*Swift/BAT* Flux (mCrab) (15 − 50 keV)	Radio Flux (mJy)	Spectral State
Cyg X−1	E1	IXPE	01002901	2022-05-15	59714.64	242	9.82 ± 0.21	401 ± 11	928 ± 34	–	LHS
		NICER	5100320101	2022-05-15	59714.26	8.2	2938 ± 25	–	–	–	–
		NuSTAR	30702017002	2022-05-18	59717.57	16	324 ± 15	–	–	–	–
		AstroSat	A11_080T01_9000005146	2022-05-15	59714.03	47.3	1505 ± 37	–	–	–	–
	E2	IXPE	01250101	2022-06-18	59748.86	86	10.32 ± 0.12	420 ± 14	885 ± 33	–	LHS
		NICER	5100320108	2022-06-20	59750.60	3	3001 ± 25	–	–	–	–
		NuSTAR	90802013002	2022-06-20	59750.50	13	338 ± 14	–	–	–	–
	E3	IXPE	02008201	2023-05-02	60066.96	21	26.93 ± 0.18	888 ± 12	546 ± 21	9.1 ± 0.3⊡	HSS
	E4	IXPE	02008301	2023-05-09	60073.44	31	33.93 ± 0.23	701 ± 12	613 ± 23	11.7 ± 0.2⊡	HSS
	E5	IXPE	02008401	2023-05-24	60088.82	25	44.26 ± 0.30	809 ± 20	569 ± 35	2.4 ± 0.2⊡	HSS
		AstroSat	T05_105T01_9000005662	2023-05-24	60088.79	60.5	1354 ± 36	–	–	–	–
	E6	IXPE	02008501	2023-06-13	60108.96	29	39.33 ± 0.28	765 ± 27	593 ± 45	8.9 ± 0.2⊡	HSS
		NuSTAR	80902318004	2023-06-14	60109.02	9.8	694 ± 22	–	–	–	HSS
	E7	IXPE	02008601	2023-06-20	60115.04	34	48.09 ± 0.24	803 ± 24	859 ± 46	9.4 ± 0.4⊡	HSS
		NICER	6643010104	2023-06-20	60115.97	7.6	23227 ± 201	–	–	–	–
		NuSTAR	80902318006	2023-06-20	60115.82	10.2	878 ± 26	–	–	–	–
	E8	IXPE	03002201	2024-04-12	60412.02	55.8	7.28 ± 0.12	333 ± 9	736 ± 31	–	LHS
		NICER	7100320104	2024-04-11	60411.10	0.7	1508 ± 18	–	–	–	–
	E9	IXPE	03003101	2024-05-06	60436.37	53.9	7.14 ± 0.11	283 ± 8	919 ± 42	–	LHS
	E10	IXPE	03010001	2024-05-26	60456.04	57.5	7.29 ± 0.12	286 ± 18	747 ± 28	–	LHS
	E11	IXPE	03010101	2024-06-14	60475.65	55.8	5.72 ± 0.09	293 ± 11	725 ± 27	–	LHS
		NICER	7706010104	2024-06-14	60475.99	6.1	1698 ± 54	–	–	–	–
	E12	IXPE	03002599	2024-10-10	60593.22	110	22.1 ± 2.2	600 ± 13	795 ± 27	–	HSS
4U 1630−47	E1	IXPE	01250401	2022-08-23	59814.95	459	4.56 ± 0.08	247 ± 8	10 ± 2	–	HSS
		NICER	5501010102	2022-08-23	59814.01	2	479 ± 10	–	–	–	–
		NuSTAR	80802313002	2022-08-25	59816.19	17	348 ± 14	–	–	–	–
	E2	IXPE	02250601	2023-03-10	60013.78	138	10.16 ± 0.12	550 ± 16	246 ± 20	–	SPL
		NICER	6557010101	2023-03-10	60013.76	5	1009 ± 15	–	–	–	–
		NuSTAR	80801327002	2023-03-09	60012.36	12	884 ± 29	–	–	–	–
		AstroSat	A12_056T02_9000005538	2023-03-10	60013.08	29.4	1938 ± 43	–	–	–	–
Cyg X−3	E1	IXPE	02001899	2022-10-14	59866.04	538	1.33 ± 0.04	106 ± 20	129 ± 26	106 ± 24*	LHS
		NICER	5142010105	2022-10-14	59866.28	5	44.79 ± 3.12	–	–	–	–
		NuSTAR	90802323002	2022-10-13	59865.62	18	197 ± 1	–	–	–	–
	E2	IXPE	02250301	2022-12-25	59938.41	199	4.55 ± 0.09	295 ± 31	144 ± 35	107 ± 36*	HSS
		NuSTAR	90801336002	2022-12-25	59938.33	36	467 ± 2	–	–	–	–
	E3	IXPE	02009101	2023-11-17	60265.83	291	1.43 ± 0.05	131 ± 8	159 ± 13	–	SIMS
		NICER	6692010101	2023-11-17	60265.77	1.9	125 ± 7	–	–	–	–
	E4	IXPE	03250301	2024-06-02	60463.77	50	7.45 ± 0.12	411 ± 16	14 ± 9	–	HSS
LMC X−1	E1	IXPE	02001901	2022-10-19	59871.61	563	0.96 ± 0.03	14 ± 9	13 ± 3	–	HSS
		NICER	5100070101	2022-10-19	59871.79	2.8	193 ± 6	–	–	–	–
		NuSTAR	90801324002	2022-10-24	59876.16	19	15 ± 2	–	–	–	–
4U 1957+115	E1	IXPE	02006601	2023-05-12	60076.10	572	1.09 ± 0.04	19 ± 4	2 ± 1	–	HSS
		NICER	6100400101	2023-05-12	60076.55	0.6	265 ± 8	–	–	–	–
		NuSTAR	30902042002	2023-05-15	60079.33	19	29 ± 4	–	–	–	–
LMC X−3	E1	IXPE	02006599	2023-07-07	60132.77	562	0.97 ± 0.03	16 ± 4	18 ± 3	–	HSS
		NICER	6101010117	2023-07-08	60133.42	0.1	358 ± 23	–	–	–	–
		NuSTAR	30902041002	2023-07-09	60134.51	28	15 ± 3	–	–	–	–
	E2	IXPE	03004899	2024-10-03	60586.51	385	1.62 ± 0.04	40 ± 5	14 ± 9	–	HSS
		NICER	7704010101	2024-10-03	60586.63	2.4	606 ± 11	–	–	–	–
	E3	IXPE	03004901	2024-11-21	60635.94	382	0.42 ± 0.02	8 ± 5	–	–	HSS
		NICER	7704010201	2024-11-23	60637.10	1.7	246 ± 7	–	–	–	–
	E4	IXPE	03005001	2025-01-11	60686.18	389	0.86 ± 0.41	11 ± 4	9 ± 7	–	HSS
		NuSTAR	31002032006	2025-01-11	60686.68	35	16 ± 5	–	–	–	

Note. †Data are not available in public domain. ⊡*AMI-LA* (15.5 GHz; J. F. Steiner et al. 2024). **RATAN* (4.7 GHz; A. Veledina et al. 2024a).

dominated state constrain LMC X−1 spin as ∼0.92 (L. Gou et al. 2009; G. R. Bhuvana et al. 2021), indicating the presence of a rapidly rotating black hole. LMC X−1 is the first source for which a null-detection of X-ray polarization has been reported from *IXPE* data (J. Podgorný et al. 2023).

• **4U 1957+115:** This is a bright and persistent low-mass X-ray binary, first discovered by the *Uhuru* mission in 1973 (R. Giacconi et al. 1974). The source distance is found to be in the range of 5–40 kpc, with inclination within ∼13°–78° and mass in ∼6–10 $M_\odot$ (D. Maitra et al. 2014; S. Gomez, P. A. Mason & E. L. Robinson 2015). Nevertheless, several studies suggest the presence of a maximally spinning black hole in 4U 1957+115 (E. Barillier et al. 2023). Polarimetric study of the source reveals several relativistic effects close to the black hole, leading to low PD of ∼1.9 per cent (L. Marra et al. 2024).

• **LMC X−3:** This is a persistent extragalactic BH-XRB in LMC at a distance of 48.1 kpc (J. A. Orosz et al. 2009), discovered by *Uhuru* in 1971. A slowly rotating black hole of spin $0.25^{+0.20}_{-0.29}$ (J. F. Steiner et al. 2010; G. R. Bhuvana et al. 2021) and mass 6.98 ± 0.56 $M_\odot$ (J. A. Orosz et al. 2014; G. R. Bhuvana et al. 2021) is found to be present at the central core of the system. LMC X−3 is a relatively high inclined system ($i \sim 69.24^\circ \pm 0.72^\circ$) (J. A. Orosz et al. (2014). Being a persistent source, it mostly remains in the HSS (G. R. Bhuvana et al. 2021) except for a few occasions during which the LHS is also observed (A. P. Smale & P. T. Boyd 2012). An exceptionally anomalous low state of peak luminosity $\sim 10^{35}$ erg s^{-1} is also observed for a few instances (T. J. Torpin et al. 2017). Interestingly, LMC X−3 is another BH-XRB for which a relatively high polarization degree (∼3 per cent) has been reported from soft state observations (S. Majumder et al. 2024a; J. Svoboda et al. 2024a).

• ***Swift* J1727.8−1613:** This is a recently discovered BH-XRB transient, first detected by *Swift*/BAT on 2023 August 24. Immediate monitoring of the source with *MAXI*/GSC in the 2–20 keV energy range revealed an 'unusual' peak in X-ray flux, increasing from 150 mCrab to 7 Crab within a few days of detection (M. Nakajima et al. 2023; A. Nandi et al. 2024). Recent measurements estimate the source distance as ∼2.7 kpc, with a spin of ∼0.98 and an inclination of ∼40° (D. Mata Sánchez et al. 2024; J.-Q. Peng et al. 2024a). X-ray polarimetric constraints with *IXPE* in various spectral states of *Swift* J1727.8–1613 also aim to unveil the disc–corona geometry of the source (A. Veledina et al. 2023; A. Ingram et al. 2024; J. Podgorný et al. 2024; J. Svoboda et al. 2024b).

• **GX 339−4:** It was discovered by the OSO−7 mission in 1973 (T. H. Markert et al. 1973) and typically undergoes outbursts every 2–3 yr. The black hole mass is constrained to be within 8.28–11.89 $M_\odot$ (H. Sreehari et al. 2019a), while the source distance is estimated as 8.4 ± 0.9 kpc (M. L. Parker et al. 2016). Recent studies suggest the source inclination angle between 30° and 34°, though spin measurements remain highly model-dependent, yielding values ranging from negative to moderate positive spins (A. A. Zdziarski et al. 2024). Further, G. Mastroserio et al. (2025) reported the alignment of X-ray polarization direction with that of radio jet orientation in GX 339–4.

• ***Swift* J151857.0−572147:** This is a newly discovered Galactic BH-XRB transient, first detected by *Swift/BAT* during its 2024 outburst (J. A. Kennea et al. 2024). Subsequent observations with *NICER* and *Insight–HXMT* constrained the source distance, inclination, and spin parameter as ∼ 5.8 kpc, ∼ 2.1°, and ∼ 0.84, respectively (J.-Q. Peng et al. 2024b). Additionally, coherent type-C QPOs were detected with *Insight–HXMT* in the intermediate state of the outburst, which have been linked to the shock instability model of transonic accretion flow around black holes (K. Chatterjee et al. 2024). Notably, S. Mondal et al. (2024) reported low polarization for this source, whereas Y.-S. Ling et al. (2024) found a null-detection.

• **IGR J17091−3624:** This is a galactic BH-XRB transient system, discovered by *INTEGRAL*/IBIS (INTErnational Gamma-Ray Astrophysics Laboratory/Imager on Board the INTEGRAL Satellite) in 2003 (E. Kuulkers et al. 2003). Interestingly, IGR J17091–3624 exhibits several exotic X-ray variability signatures, including the well known 'heartbeat' class and therefore, often termed as the twin of GRS 1915+105 (F. Capitanio et al. 2012; D. Radhika et al. 2018; T. Katoch et al. 2021; Q.-C. Shui et al. 2024; J. Wang et al. 2024). Using reflection spectroscopy, the inclination of the source is estimated as ∼30°–45° (Y. Xu et al. 2017; Y. Wang et al. 2018). In addition, spectral modeling suggests a black hole of mass 10–12.3 $M_\odot$ likely to be present at the centre of IGR J17091–3624 (N. Iyer et al. 2015; D. Radhika et al. 2018). Based on the luminosity estimates, the distance of the source is predicted to lie within 11–17 kpc (J. Rodriguez et al. 2011). Further, exceptionally high polarization degree has been reported for this source in LHS (D. Debnath, S. Srimani & H.-K. Chang 2025; M. Ewing et al. 2025).

• **MAXI J1744−294:** The sources is located near the Galactic centre, is the most recently discovered X-ray transient by *MAXI*/GSC on 2025 January 2, at a flux level of ∼133 mCrab (Y. Kudo et al. 2025). The energy spectra of the source, obtained from follow-up *NuSTAR* observations, are found to be well described with the model comprising a thermal disc component of temperature ∼ 0.7 keV, a power-law component of photon index ∼ 2.3, and iron line profile at ∼ 6.6 keV (S. Mandel et al. 2025). Based on these initial findings, the source is inferred to be a BH-XRB transient observed in the HSS (S. Mandel et al. 2025). Assuming a distance of 8 kpc, the luminosity of the source is estimated to be $\sim 1.5 \times 10^{37}$ erg s^{-1} in 2–10 keV energy range (S. Mandel et al. 2025).

3 DATA REDUCTION

IXPE, NASA's first space-based low-energy X-ray polarimetry mission, was launched on 2021 December 9 (M. C. Weisskopf et al. 2022). It comprises three identical gas-pixel detector units (DUs) designed to measure the polarimetric properties of astrophysical sources using the principle of photoelectron tracking in the 2–8 keV energy band. For each detected photon, the Stokes parameters (I, Q, U) are determined based on the azimuthal angle of the electric field vector, which is reconstructed by analysing the photoelectron track within the detector plane. The additive nature of the Stokes parameters enables the summation of individual photon contributions to obtain the resultant I, Q, and U, which are used to calculate the PD and PA.

For the polarimetric analysis, we utilize the cleaned and calibrated level-2 event files from the three DUs of *IXPE* in the 2–8 keV energy range. Data reduction is performed using the latest IXPEOBSSIMV31.0.3 software (L. Baldini et al. 2022), following standard procedures outlined in F. Kislat et al. (2015), T. E. Strohmayer (2017), A. Kushwaha et al. (2023), and S. Majumder et al. (2024a, b). The source and background regions are defined as a 60 arcsec circular region centred at the source coordinates and an annular region with radii between 180 and 240 arcsec, respectively (A. Kushwaha et al. 2023; S. Majumder et al. 2024a). The XPSELECT task is used to extract source and background events from these regions. We use XPBIN task with various algorithms, such as PCUBE, PHA1, PHA1Q, and PHA1U, to generate the necessary data products for model-dependent polarization as well as spectro-polarimetric studies, respectively. The latest response files provided by the

software team are used in the fitting of Stokes spectra. The *IXPE* light curves of 2000 s time bin are extracted from the event files using XSELECT.

NICER (K. C. Gendreau et al. 2016) is the X-ray mission onboard the International Space Station (ISS), sensitive in the soft X-ray energy band of 0.2 –12 keV and capable of excellent observations for in-depth spectro-temporal studies. The *NICER*/XTI data are reduced using the standard data extraction software (NICERDASV13) integrated within HEASOFT V6.34 with the appropriate calibration data base. We use the tool NICERL2 with standard filtering criteria to generate the clean event files. The spectral products are generated using the task `nicerl3-spect` with background model `3c50` (R. A. Remillard et al. 2022). The *NICER* light curves of desired time resolutions are generated using `nicerl3-lc` task.

We analyse the *NuSTAR* (F. A. Harrison et al. 2013) data using the dedicated software NUSTARDAS available in HEASOFT V6.34. We use the task NUPIPELINE to generate the cleaned event files from both FPMA (Focal Plane Module A) and FPMB (Focal Plane Module B) instrument onboard *NuSTAR*.A circular region of 60 arcsec radii at the source position and away from it is considered to extract the source and background spectra, instrument response and ancillary files, respectively, using the task NUPRODUCT. All the *NuSTAR* spectra are grouped with 25 counts per bin to obtain better statistics during the spectral fitting.

AstroSat (P. C. Agrawal 2006) data are extracted using the latest reduction software LAXPCSOFTV3.4.4. The standard procedures of *AstroSat*/LAXPC data extraction are performed following H. M. Antia et al. (2017, 2021, 2022), H. Sreehari et al. (2019b, 2020), and S. Majumder et al. (2022). We use LAXPC20 data for generating the light curves in different energy ranges for the respective sources except *Swift* J1727.8–1613, for which LAXPC10 data in low gain mode were available for analysis (see A. Nandi et al. 2024, for details). Note that, level-1 data corresponding to single events from all layers of the detector are considered in each observation.

We utilize on-demand[3] processed *MAXI*/GSC (M. Matsuoka et al. 2009) data and scaled map transient analysis data[4] of *Swift*/BAT (H. A. Krimm et al. 2013) for the individual sources in different energy ranges. Note that, *MAXI*/GSC count rates in 2–20 keV energy range are converted into the flux unit (Crab) following the relation 1 Crab = 3.8 photons cm^{-2} s^{-1} as suggested by the instrument team.[5] Similarly, for *Swift*/BAT data in the 15–50 keV energy range, we obtain the corresponding photon flux[6] in units of mCrab, where 1 mCrab = 0.000220 counts cm^{-2} s^{-1}.

4 ANALYSIS AND RESULTS

4.1 Temporal analysis

4.1.1 Multimission monitoring

We study the variability properties of each source using multimission data during the epochs of *IXPE* observations. In Fig. 1, we present the count rate obtained with *MAXI*/GSC (2–20 keV) and *Swift*/BAT (15–50 keV) monitoring in panels (a) and (b) along with the variation of hardness ratio (HR) from *MAXI*/GSC in panel (c), respectively, for all sources under consideration. Here, HR is defined as the flux ratio in 6–20 and 2–6 keV. Note that, flux values associated with the count rates in soft (hard) energy bands with *MAXI*/GSC *(Swift*/BAT*)* are also mentioned in units of mCrab in the y-axis (right side) of the respective panels. Further, radio flux densities obtained from different observational campaigns, such as *RATAN* (Radio Astronomical Telescope of the Academy of Sciences) (A. Ingram et al. 2024; A. Veledina et al. 2024a), *E-MERLIN* (enhanced Multi-Element Radio Linked Interferometer Network) (D. Williams-Baldwin et al. 2023), *VLITE* (VLA Low-Band Ionosphere and Transient Experiment) (W. M. Peters et al. 2023), and *AMI-LA* (Arcminute Microkelvin Imager Large Array) (J. F. Steiner et al. 2024) near the *IXPE* epochs, are shown in panel (d) for the respective sources based on their availability.We observe that all sources show marginal variation in both *MAXI*/GSC and *Swift*/BAT count rates over the entire *IXPE* exposure for a given epoch. Hence, in Fig. 1(a–c), we present the average values of the respective quantities over the entire *IXPE* exposure of each epoch.

Interestingly, for *Swift* J1727.8–1613, we observe that both *MAXI*/GSC and *Swift*/BAT flux decrease as its outburst progresses. The HR also sharply decreases and anticorrelates with the accompanied radio flux density (see Fig. 1c–d). The variation of both low and high energy fluxes along with HR in presence of radio ejection suggest that the source evolves through spectral state transitions. In particular, we notice exceptionally bright ($\gtrsim$ 3 Crab) intermediate states ($HR \sim$ 0.1–0.5, E1–E5) followed by relatively faint ($\sim$ 30 mCrab) softer states ($HR \sim$ 0.04–0.1, E6–E7) before the appearance of dimmed ($\sim$100 mCrab) hard state ($HR \sim$ 0.3, E8) (see Table 2). Moreover, these variability features resemble the 'canonical' state transition as HIMS $\rightarrow$ SIMS $\rightarrow$ HSS $\rightarrow$ LHS (decay), commonly exhibited by BH-XRB transients (see A. Nandi et al. 2012, for details). Similarly, for Cyg X−1, we observe a marginal increase in the *MAXI*/GSC count rate and a corresponding decrease in the *Swift*/BAT count rate during epochs E3 to E7. In the subsequent observations (E8 to E11), the *MAXI*/GSC count rate decreases while the *Swift*/BAT count rate rises. In addition, HR shows a significant drop from 0.4 to 0.1 followed by an increase in values exceeding 0.4. This trend possibly indicates the spectral state transitions between LHS (E1–E2, E8–E11) and HSS (E3–E7, E12), respectively (see Table 1).

However, only marginal variations are seen in both low- and high-energy count rates for several sources, such as LMC X−1, LMC X−3, 4U 1957+115, GX 339–4, *Swift* J151857.0–572147, and MAXI J1744–294. For all of them, the HR remains low ($HR \lesssim 0.1$) and these sources are also detected at flux levels below approximately 100 mCrab. These possibly suggest that the sources are likely in softer spectral states. In contrast, Cyg X−3 exhibits a clear sequence of state transitions, evolving from the LHS to the HSS, then to the SIMS, and back to HSS. This evolution is accompanied by moderate changes in count rates and hardness ratio, and is likely associated with strong radio flares ($\sim$100 mJy) (see Table 1, Fig. 1, and A. Veledina et al. 2024a). For 4U 1630–47, HSS (A. Kushwaha et al. 2023) and SPL (N. Rodriguez Cavero et al. 2023) states are observed with reasonable variations in the count rates and HR. It is worth noting that IGR 17091–3624 is observed in the LHS at $\sim$1 Crab *MAXI*/GSC flux with $HR \sim$ 0.4, very similar to the LHS observations of Cyg X−1. Furthermore, GRS 1915+105 is observed with *IXPE* in its present faint and obscured state with a flux level of $\sim$6 mCrab only (see Fig. 1). We find that observations in harder spectral states (LHS and HIMS) and relatively softer spectral states (HSS, SIMS, and SPL) of the sources are separated in two distinct regions of HR variations (see Fig. 1). In particular, $HR \sim 0.22$ separates two regions, with $HR > 0.22$ indicating harder and $HR < 0.22$ corresponds to softer spectral states with few exceptions.

[3] http://maxi.riken.jp/mxondem/
[4] https://swift.gsfc.nasa.gov/results/transients/
[5] http://maxi.riken.jp/top/readme.html
[6] https://swift.gsfc.nasa.gov/results/transients/

Table 2. Same as Table 1.

Source	Epoch	Instrument	Obs. ID	Start Date	MJD Start	Exposure (ks)	Mean Rate (cts/s)	*MAXI/GSC* Flux (mCrab) (2 – 20 keV)	*Swift/BAT* Flux (mCrab) (15 – 50 keV)	Radio Flux (mJy)	Spectral State
Swift J1727.8−1613	E1	IXPE	02250901	2023-09-07	60194.81	19	42.21 ± 0.28	6053 ± 71	4898 ± 173	$120 \pm 12^{**}$	HIMS
		NICER	6203980115	2023-09-08	60195.61	0.2	64955 ± 274	–	–	–	–
		NuSTAR	80902333006	2023-09-07	60194.78	0.7	6536 ± 8	–	–	–	–
		AstroSat	T05_145T01_9000005836	2023-09-08	60195.07	32	541 ± 23	–	–	–	–
	E2	IXPE	02251001	2023-09-16	60203.70	37	41.29 ± 0.25	5058 ± 31	2472 ± 98	$144 \pm 4.32^{*}$	HIMS
		NICER	6203980119	2023-09-13	60200.18	4.9	65392 ± 122	–	–	–	–
		NuSTAR	80902313002	2023-09-16	60203.81	0.6	5478 ± 26	–	–	–	–
	E3	IXPE	02251101	2023-09-27	60214.92	21	36.85 ± 0.22	3395 ± 49	300 ± 10	$88 \pm 2.64^{*}$	HIMS
	E4	IXPE	02251201	2023-10-04	60221.54	17	41.31 ± 0.24	4689 ± 46	206 ± 38	$11 \pm 0.33^{*}$	SIMS
		NICER	6557020401	2023-10-04	60221.18	6.5	66263 ± 62	–	–	–	–
		NuSTAR	80902313008	2023-10-04	60221.54	0.5	4111 ± 4	–	–	–	–
	E5	IXPE	02251301	2023-10-10	60227.47	18	34.62 ± 0.20	3446 ± 38	206 ± 38	$35 \pm 1.05^{*}$	SIMS
		NICER	6203980136	2023-10-09	60226.02	1.9	57789 ± 149	–	–	–	–
		NuSTAR	80902313016	2023-10-10	60227.82	1.1	3196 ± 4	–	–	–	–
	E6	IXPE	03005701	2024-02-11	60351.39	67	8.09 ± 0.13	80 ± 7	21 ± 12	–	HSS
		NICER	7708010101	2024-02-11	60351.39	3.1	6415 ± 37	–	–	–	–
	E7	IXPE	03006001	2024-02-20	60360.07	151	5.59 ± 0.09	67 ± 8	26 ± 22	–	HSS
		NICER	7708010106	2024-02-19	60359.07	0.6	5354 ± 34	–	–	–	–
	E8	IXPE	03005801	2024-04-03	60403.66	202	7.87 ± 0.11	76 ± 11	109 ± 14	–	LHS
		NICER	7708010109	2024-04-03	60403.29	2.5	675 ± 12	–	–	–	–
GX 339 − 4	E1	IXPE	03005101	2024-02-14	60354.93	95	17.44 ± 0.21	–	79 ± 25	–	SIMS
		NICER	7702010112	2024-02-14	60354.98	3.8	5263 ± 34	–	–	–	–
		NuSTAR	91002306002	2024-02-14	60354.70	16	308 ± 13	–	–	–	–
		AstroSat	A05_166T01_9000006070	2024-02-14	60354.31	50.7	629 ± 26	–	–	–	–
	E2	IXPE	03005301	2024-03-08	60377.68	98	7.37 ± 0.11	103 ± 6	12 ± 8	–	HSS
		AstroSat†	A13_028T01_9000006122	2024-03-10	60379.44	–	–	–	–	–	–
Swift J151857.0 − 572147	E1	IXPE	03250201	2024-03-18	60387.15	96	12.18 ± 0.12	422 ± 8	152 ± 17	–	HSS
		NICER	7204220111	2024-03-18	60387.55	4.2	1468 ± 18	–	–	–	–
		NuSTAR	91001311004	2024-03-18	60387.64	9.2	444 ± 17	–	–	–	–
IGR J17091 − 3624	E1	IXPE	04250201	2025-03-07	60741.30	163	0.27 ± 0.02	755 ± 11	82 ± 27	–	LHS
		NuSTAR	81002342008	2025-03-07	60741.58	21	27 ± 15	–	–	–	–
MAXI J1744 − 294	E1	IXPE	04250301	2025-04-05	60770.09	149	0.17 ± 0.11	45 ± 28	–	–	HSS
GRS 1915 + 105	E1	IXPE	04003501	2025-05-10	60805.69	142	–	6 ± 3	–	–	–

Note. †Data are not available in public domain. **RATAN* (4.7 GHz; A. Veledina et al. 2023; A. Ingram et al. 2024); ***E-MERLIN* (5.1 GHz; D. Williams-Baldwin et al. 2023).

4.1.2 *Power density spectra*

We investigate the PDS of all sources in different spectral states using *NICER* observations (see Table 1) in 0.5–10 keV energy range. In addition, PDS properties in hard X-rays (>10 keV) are also examined using available *NuSTAR* and *AstroSat* observations of the sources. We generate 0.01 s time binned light curves and compute the PDS up to Nyquist frequency of 50 Hz with 1024 newbins per interval using POWSPEC inside HEASOFT V6.34. The individual power spectra are averaged out to get the resultant PDS in units of rms^2/Hz which is geometrically rebinned in the frequency space with a factor of 1.03 (see T. Belloni, D. Psaltis & M. Klis 2002; T. Belloni et al. 2005; H. Sreehari et al. 2019b; S. Majumder et al. 2022). In the upper panels of Fig. 2, we present the PDS of the respective sources in different spectral states. We model each PDS with a combination of `constant` and multiple `Lorentzian` components. Further, we compute the total percentage rms amplitude ($rms_{\rm tot}$%) as a measure of variability in 0.1–50 Hz and tabulate it in Table 3.

Interestingly, we observe that the PDS in several spectral states exhibit distinct variable features. In particular, PDS of Cyg X−1 in the LHS show significant variability with $rms_{\rm tot}\% \sim 31.1 - 52.4$ (0.5–10 keV) and a clear power spectral break at ~ 1.5 Hz with *NICER* observations. Further, power spectral properties in hard X-rays (3–80 keV) with quasi-simultaneous *AstroSat* observations exhibit similar break frequencies (~ 1.5 Hz) with $rms_{\rm tot}\% \sim 37$ in LHS (see Table 1 and Fig. 2a). We also observe marginal (significant) PDS variability of $rms_{\rm tot}\% \sim 9.1$ (33) with low (high) energy *NICER* (*AstroSat*) observations of Cyg X−1 in the HSS. Note that similar variability properties including power spectral breaks were also reported by A. Kushwaha et al. (2021) in LHS and HSS of Cyg X−1.

For *Swift* J1727.8–1613, the presence of type-C QPO feature at ~ 1.4 Hz is observed during HIMS (epoch 1, hereafter E1) in 0.5–100 keV with *NICER*, *NuSTAR*, and *AstroSat* quasi-simultaneous observations (see also A. Nandi et al. 2024; J. Liao et al. 2024). The evolution of the QPO frequency up to ~ 6.7 Hz is seen with *NICER* in the later epochs (E2–E5). However, a power distribution, similar to Cyg X−1 (LHS), is observed in the LHS of *Swift* J1727.8–1613 without the presence of power spectral break, whereas marginal variability with $rms_{\rm tot}\% \sim 1.4$ is noticed during HSS (E6–E7).

The remaining sources (4U 1630–47, LMC X−1, LMC X−3, 4U 1957+115, Cyg X−3, and *Swift* J151857.0–572147) in SIMS and HSS display weak variability signatures mostly represented by constant noise distribution and occasionally marginal power variation at lower frequencies. Conversely, during the recurrent outburst of GX 339–4, a sharp type-B QPO peak at ~ 4.5 Hz ($rms_{\rm QPO}\% \sim 10.2$)

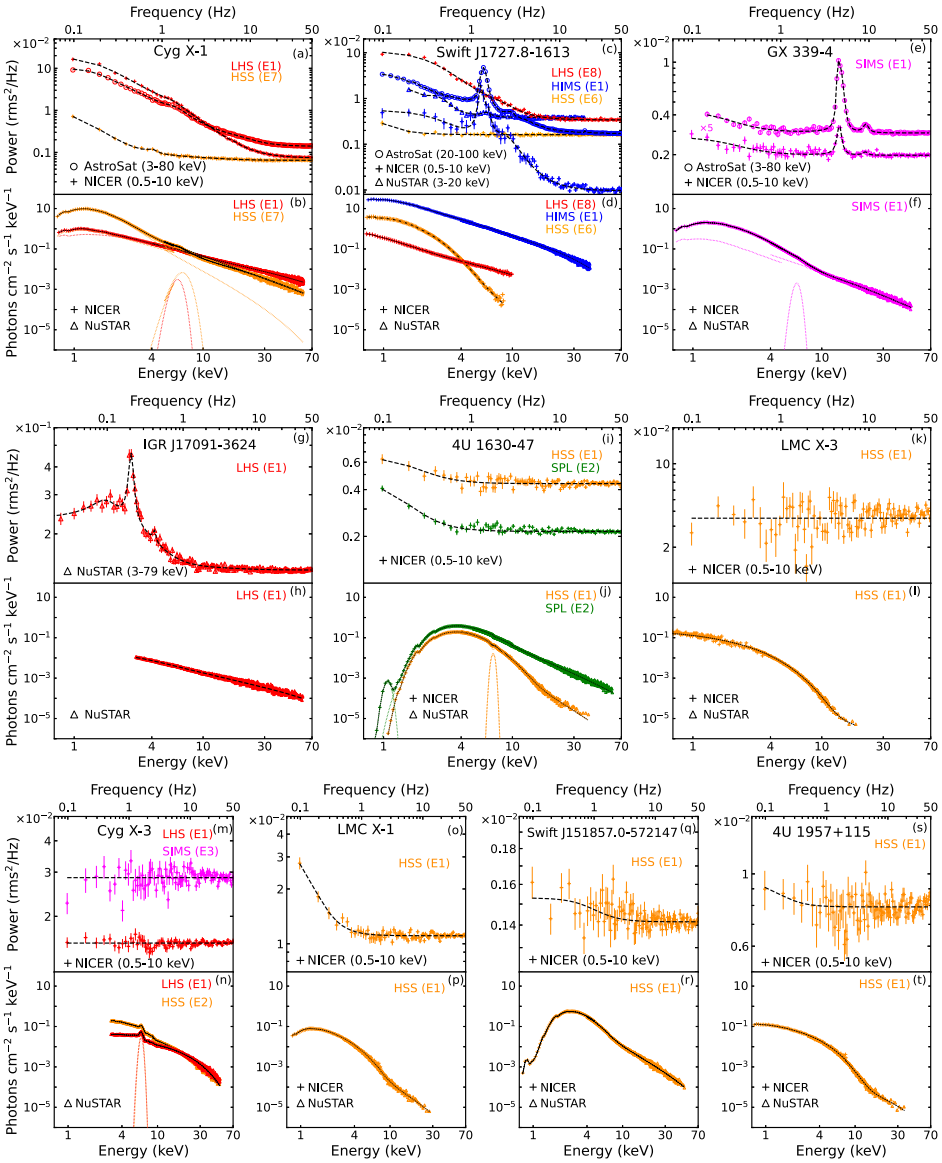

Figure 2. Results of temporal (top panel) and spectral (bottom panel) analyses of 10 BH-XRBs in different spectral states (colour coded) obtained using quasi-simultaneous *IXPE*, *NICER*, *NuSTAR*, and *AstroSat* observations. *Top panels:* PDS obtained from *NICER* (0.5–10 keV) and/or *NuSTAR*/*AstroSat* observations in different energy ranges are depicted for the respective sources in various epochs. The power spectrum of GX 339–4 from *NICER* observation is rescaled by a factor of 5. *Bottom panels:* Energy spectra of the sources from *NICER* and/or *NuSTAR* data are shown during the respective epochs. PDS and energy spectra in LHS, HIMS, SIMS, HSS, and SPL states are presented using red, blue, magenta, orange, and green colours, respectively. PDS from *NuSTAR* and *AstroSat* data are plotted using circle and triangle, irrespective of the spectral states. See the text for details.

and harmonic feature at ~ 9.5 Hz along with weak broad-band noise ($rms_{\rm tot}\% \sim 15.4$) are observed in SIMS (see Fig. 2 and U. Aneesha et al. 2024). Note that, the QPO features with enhanced $rms_{\rm QPO}\%$ from 3.76 (0.5–10 keV) to 12.6 (3–80 keV) are observed with *NICER* and *AstroSat*, respectively. For IGR J17091–3624, a sharp type-C QPO at ~ 0.2 Hz ($rms_{\rm QPO}\% \sim 15$) along with a weak harmonic at ~ 0.4 Hz are observed during the recent outburst (see Fig. 2).

Moreover, the overall power spectral properties of the sources, including break frequencies, noise distribution, and the detection of type-C and type-B QPO features confirm the presence of distinct spectral states during the respective *IXPE* campaigns. These findings further corroborate the results indicating distinct spectral states, obtained from the multimission monitoring of the sources (see Section 4.1.1).

4.2 Wide-band spectral analysis

4.2.1 *Spectral modelling*

We investigate the wide-band (0.7–60 keV) spectral characteristics of each source using quasi-simultaneous *NICER* and *NuSTAR* observations. Depending on the availability of spectral coverage from different instruments, the spectra are modelled in different energy ranges (see Table 3). For some observations, the spectra at higher energies are seen to be background dominated and/or of large uncertainties. Accordingly, we remove those parts of the spectra and proceed for modelling. To start with, we adopt the model combination `constant×Tbabs×(thcomp⊗diskbb)` (hereafter `M1`) comprising of a convolution thermal Comptonization component

Table 3. Results from the wide-band spectral analysis of 10 BH-XRBs using *NICER* and *NuSTAR* data, modelled with `M1 : constant×Tbabs×(thcomp⊗diskbb)`, unless stated otherwise. Here, $n_{\rm H}$, $kT_{\rm in}$, $kT_{\rm e}$, $\Gamma_{\rm th}$, and $cov_{\rm frac}$ denote the column density, inner disc temperature, electron temperature, photon index, and covering fraction, respectively. $F_{\rm disc}$, $F_{\rm Comp}$, and $F_{\rm bol}$ represent the disc, Comptonized, and total bolometric fluxes, respectively. $L_{\rm bol}$ indicates the bolometric luminosity. $rms_{\rm tot}$ corresponds to the rms amplitude derived from the respective PDS. The energy ranges used for each spectrum and the associated spectral states are also mentioned. See the text for details.

Source	Epoch	$n_{\rm H}$ (10^{22} cm^{-2})	$kT_{\rm in}$ (keV)	$kT_{\rm e}$ (keV)	$\Gamma_{\rm th}$	$cov_{\rm frac}$	$\chi^2/d.o.f$	$F_{\rm disc}$ [a]	$F_{\rm Comp}$ [a] (10^{-8} erg cm^{-2} s^{-1})	$F_{\rm bol}$ [a]	$L_{\rm bol}$ [a] (%$L_{\rm Edd}$)	Spectral State	Energy range (keV)	$rms_{\rm tot}$ [b] (%)
Cyg X−1	E1	$0.44^{+0.02}_{-0.02}$	$0.41^{+0.03}_{-0.03}$	$30.35^{+2.87}_{-2.22}$	$1.61^{+0.02}_{-0.01}$	$0.77^{+0.02}_{-0.02}$	1517/1468	0.68	2.45	3.07	1.4	LHS	0.7 − 60	32.5
($d = 2.2$ kpc)	E2	$0.34^{-0.02}_{-0.02}$	$0.38^{+0.01}_{-0.01}$	$22.57^{+1.50}_{-1.13}$	$1.61^{+0.01}_{-0.01}$	$0.73^{+0.04}_{-0.03}$	1479/1403	0.74	2.53	3.29	1.5	LHS	0.7 − 60	31
	E6[c]	0.51 [d]	$0.52^{+0.02}_{-0.02}$	10 [d]	1.01 [d]	$0.005^{+0.002}_{-0.002}$	2122/1913	1.75	0.22	4.43	2	HSS	3 − 60	–
	E7 [c]	$0.52^{+0.01}_{-0.01}$	$0.43^{+0.02}_{-0.01}$	10 [d]	$3.21^{+0.11}_{-0.14}$	$0.31^{+0.03}_{-0.02}$	2185/2167	3.78	0.33	6.18	2.8	HSS	0.7 − 60	9.1
	E8	$0.43^{+0.03}_{-0.03}$	$0.27^{+0.03}_{-0.03}$	20 [d]	$1.64^{+0.02}_{-0.02}$	$0.65^{+0.06}_{-0.07}$	115/133	0.37	1.15	1.53	0.7	LHS	0.7 − 10	41.5
	E11	$0.39^{+0.02}_{-0.04}$	$0.32^{+0.03}_{-0.04}$	20 [d]	$1.62^{+0.03}_{-0.03}$	$0.61^{+0.04}_{-0.04}$	152/131	0.39	1.18	1.58	0.7	LHS	0.7 − 10	52.4
4U 1630−47	E1	$6.69^{+0.24}_{-0.30}$	$1.36^{+0.01}_{-0.01}$	20 [d]	$3.34^{+0.12}_{-0.11}$	$0.052^{+0.008}_{-0.007}$	1134/928	1.56	0.03	1.59	15.1	HSS	0.7 − 40	6.7
($d = 10$ kpc)	E2	$4.55^{+0.07}_{-0.05}$	$1.46^{+0.02}_{-0.02}$	20 [d]	$2.47^{+0.05}_{-0.04}$	$0.38^{+0.02}_{-0.01}$	2366/1980	2.76	0.77	3.65	34.7	SPL	0.7 − 60	4.8
Cyg X−3	E1	$4.04^{+0.26}_{-0.11}$	$1.21^{+0.02}_{-0.02}$	$6.14^{+0.28}_{-0.34}$	$1.55^{+0.03}_{-0.04}$	$0.83^{+0.02}_{-0.01}$	2921/1842	0.21	0.41	0.64	5.7	LHS	3 − 50	–
($d = 9.7$ kpc)	E2	$5.54^{+0.07}_{-0.13}$	$1.01^{+0.01}_{-0.02}$	$7.95^{+0.22}_{-0.14}$	$2.21^{+0.01}_{-0.01}$	$0.63^{+0.01}_{-0.01}$	2709/1903	0.94	0.62	1.58	14.1	HSS	3 − 50	–
LMC X−1	E1	$0.50^{+0.01}_{-0.01}$	$0.98^{+0.01}_{-0.01}$	10 [d]	$2.58^{+0.10}_{-0.09}$	$0.091^{+0.012}_{-0.010}$	744/613	0.065	0.004	0.074	16	HSS	0.8 − 30	10.1
($d = 48.1$ kpc)														
4U 1957+115	E1	$0.08^{+0.01}_{-0.01}$	$1.40^{+0.01}_{-0.01}$	10 [d]	$1.86^{+0.12}_{-0.10}$	$0.027^{+0.004}_{-0.004}$	728/701	0.092	0.005	0.096	0.9	HSS	0.7 − 40	5
($d = 10$ kpc)														
LMC X−3	E1	0.04 [d]	$1.10^{+0.01}_{-0.01}$	10 [d]	$1.78^{+0.45}_{-0.35}$	$0.005^{+0.003}_{-0.002}$	567/543	0.061	0.001	0.062	13.4	HSS	0.7 − 20	–
($d = 48.1$ kpc)	E2	0.04 [d]	$1.09^{+0.01}_{-0.01}$	10 [d]	$2.51^{+0.08}_{-0.07}$	0.3 [d]	153/128	0.11	0.03	0.14	30.8	HSS	1 − 10	–
	E3	0.04 [d]	$0.6^{+0.04}_{-0.03}$	$1.04^{+0.08}_{-0.05}$	$1.72^{+0.11}_{-0.08}$	0.4 [d]	118/117	0.03	0.006	0.035	7.7	HSS	1 − 10	–
	E4	0.04 [d]	$1.07^{+0.01}_{-0.01}$	10 [d]	$2.05^{+0.05}_{-0.04}$	$0.005^{+0.003}_{-0.003}$	771/706	0.06	0.006	0.07	15.4	HSS	3 − 30	–
Swift J1727.8−1613	E1	$0.23^{+0.01}_{-0.01}$	$0.29^{+0.01}_{-0.02}$	$8.44^{+0.16}_{-0.11}$	$1.98^{+0.04}_{-0.02}$	$0.74^{+0.01}_{-0.01}$	1181/931	10.07	15.01	25.24	17.5	HIMS	0.7 − 40	12
($d = 2.7$ kpc)	E2	$0.20^{+0.01}_{-0.01}$	$0.43^{+0.02}_{-0.02}$	$9.34^{+0.22}_{-0.23}$	$2.11^{+0.05}_{-0.04}$	$0.82^{+0.02}_{-0.02}$	912/847	11.35	13.58	25.11	17.4	HIMS	0.7 − 40	–
	E4 [c]	$0.25^{+0.01}_{-0.01}$	$0.85^{+0.03}_{-0.02}$	10[d]	$2.74^{+0.04}_{-0.04}$	$0.38^{+0.04}_{-0.03}$	1373/1447	15.89	3.63	25.04	17.3	SIMS	0.7 − 40	6.1
	E5 [c]	$0.29^{+0.02}_{-0.01}$	$0.88^{+0.02}_{-0.02}$	10 [d]	$2.32^{+0.06}_{-0.04}$	$0.19^{+0.02}_{-0.02}$	1572/1601	10.12	2.09	16.78	11.6	SIMS	0.7 − 60	6.4
	E6	$0.17^{+0.01}_{-0.01}$	$0.48^{+0.01}_{-0.01}$	10 [d]	$5.14^{+0.36}_{-0.39}$	$0.17^{+0.03}_{-0.05}$	127/132	0.91	0.02	0.93	0.6	HSS	0.7 − 10	1.4
	E7	$0.18^{+0.01}_{-0.01}$	$0.45^{+0.01}_{-0.01}$	10 [d]	$4.57^{+0.65}_{-0.60}$	$0.13^{+0.09}_{-0.05}$	102/111	0.66	0.01	0.67	0.5	HSS	0.7 − 10	1.3
	E8	0.12 [d]	$0.24^{+0.01}_{-0.01}$	20 [d]	$1.71^{+0.03}_{-0.02}$	$0.35^{+0.01}_{-0.01}$	126/130	0.08	0.12	0.19	0.1	LHS	0.7 − 10	30.2
GX 339–4	E1[c]	$0.51^{+0.01}_{-0.01}$	$0.60^{+0.02}_{-0.02}$	$0.97^{+0.02}_{-0.01}$	$2.02^{+0.44}_{-0.52}$	$0.34^{+0.08}_{-0.05}$	1603/1538	0.84	0.36	1.71	11.5	SIMS	0.7 − 50	14.2
($d = 8.4$ kpc)														
Swift J15187.0–572147	E1	$3.83^{+0.02}_{-0.01}$	$0.94^{+0.01}_{-0.01}$	20 [d]	$2.50^{+0.01}_{-0.01}$	$0.21^{+0.01}_{-0.01}$	1572/1367	2.11	0.34	2.71	8.7	HSS	0.7 − 50	12.6
($d = 5.8$ kpc)														
IGR J17091–3624	E1	1.1 [d]	$0.88^{+0.27}_{-0.38}$	$23.54^{+4.01}_{-2.91}$	$1.62^{+0.02}_{-0.01}$	$0.87^{+0.03}_{-0.03}$	1465/1486	0.02	0.13	0.15	1.7	LHS	3 − 60	24.3
($d = 11$ kpc)														

Note. $L_{\rm Edd} = 1.26 \times 10^{39}$ erg s^{-1} for 10 $M_\odot$ BH.
[a] Calculated in 1–100 keV energy range.
[b] Computed in 0.1–50 Hz using *NICER* observations in 0.5–10 keV energy range.
[c] Results are obtained using model `M3`.
[d] Frozen values.

thcomp (A. A. Zdziarski et al. 2020) along with the standard disc component diskbb (K. Makishima et al. 1986). Here, Tbabs (J. Wilms, A. Allen & R. McCray 2000) accounts for the intergalactic absorption column density and the local absorption to the source. Note that, the component thcomp relies on the assumption of spherical geometry of the Comptonizing corona as the source of hot thermal electrons and up-scatters a fraction of the seed photon distribution of diskbb into higher energies. The model thcomp includes a parameter known as the covering fraction ($cov_{\rm frac}$), which represents the fraction of soft photons that are Comptonized in the corona. Consequently, $1 - cov_{\rm frac}$ represents the photon fraction that escape to the observer without undergoing Comptonization. The constant is used to adjust the cross-calibration between the spectra of different instruments wherever applicable. With this, the model M1 is found to provide the best description of the spectra for all sources except a few observations of Cyg X−1 (E6 and E7), *Swift* J1727.8–1613 (E4 and E5), and GX 339–1 (E1), which are discussed in the next section. Additionally, we note that a partial covering fraction absorption component pcfabs and a Gaussian absorption line gabs are required to model the low energy absorption features and the disc–wind regulated absorption line at ~ 7 keV, seen in the spectra of 4U 1630−47 during epoch-E1. Further, we use Gaussian components at ~ 1.8 keV and ~ 2.2 keV (A. Kushwaha et al. 2023) to account for the instrumental features of *NICER* and at ~ 1 keV for the possible low energy emission line, depending on the strength of the lines in different observations. We also use Gaussian line at ~ 6.4 keV in several observations to account for the prominent iron Kα line emission. It may be noted that the *NICER* spectra of Cyg X−3 exhibit multiple emission lines at various energies, which restricts us from constraining the parameters of model M1. Therefore, we use the *NuSTAR* data only in the spectral study of Cyg X−3. Further, the convolution model cflux is used without Tbabs component to estimate the bolometric flux associated with each model component and the entire spectral flux in 1–100 keV energy range. Using the estimated distance of each source (see Table 3), we compute the bolometric luminosity in units of Eddington luminosity. The best-fitting wide-band spectra (using M1) in different energy ranges and spectral states for the respective sources are shown in bottom panels of Fig. 2.

4.2.2 *Alternative spectral models*

We aim to explore the possible alternative disc–corona geometries in explaining the high-energy tail of the observed spectra. To achieve this, we use the comptt (L. Titarchuk 1994) component as a proxy for thcomp in modelling thermal Comptonization. Note that, the 'geometry switch' selected inside comptt model as '≤ 1' enables a disc-like geometry for the Comptonizing corona. Considering this, we proceed in the spectral fitting of all sources with the model combination constant×Tbabs×(diskbb + comptt) (hereafter M2). Interestingly, we find that the model M2 provides a fit equally as good as M1 for all observations under consideration except a few observations of Cyg X−1 (E6 and E7), *Swift* J1727.8–1613 (E4 and E5) and GX 339–4 (E1). This leads to a possible degeneracy between the selected models in describing the observed spectra and the geometry of the Comptonizing region.

It is worth noting that both M1 and M2 model combinations fail to provide a satisfactory fit to the observed spectra of Cyg X−1 (E6 and E7), *Swift* J1727.8–1613 (E4 and E5) and GX 339–4 in the HSS/SIMS, resulting in a $\chi^2_{\rm red} \sim 2.7 - 13$ (for M1). This is mostly due to the presence of strong reflection features including iron Kα line profile at ~ 6.4 keV and reflection hump at ~ 30 keV. To fit these reflection features, we include relxill (J. García et al. 2014) component to model M1. Note that, relxill assumes an empirical power law to model the emissivity profile of the corona of arbitrary geometry and calculates the primary spectrum considering a cutoffpl profile. With this, the model combination constant×Tbabs×(thcomp⊗diskbb + relxill) (hereafter M3) delineates the spectral data in the HSS/SIMS of Cyg X−1, *Swift* J1727.8–1613, and GX 339–4 with significant improvement in $\chi^2_{\rm red}$ in the range $\sim 0.95 - 1.11$. A Gaussian at ~ 6.5 keV is also required along with the components of M3 to obtain the best fit for Cyg X−1 and GX 339–4 observations. We fix the spin and inclination of the sources to the previously estimated values reported in A. Kushwaha et al. (2021), J.-Q. Peng et al. (2024a), and G. Mastroserio et al. (2025), during the spectral fitting. In Fig. 3, we depict the variation of the ratio of data to fitted model (M1 and M3) for these sources, which indicates significant improvement of the respective fits by incorporating reflection component. We state that, M3 fails to assert its relevance to the spectra of other sources in different states due to the absence of prominent reflection features.

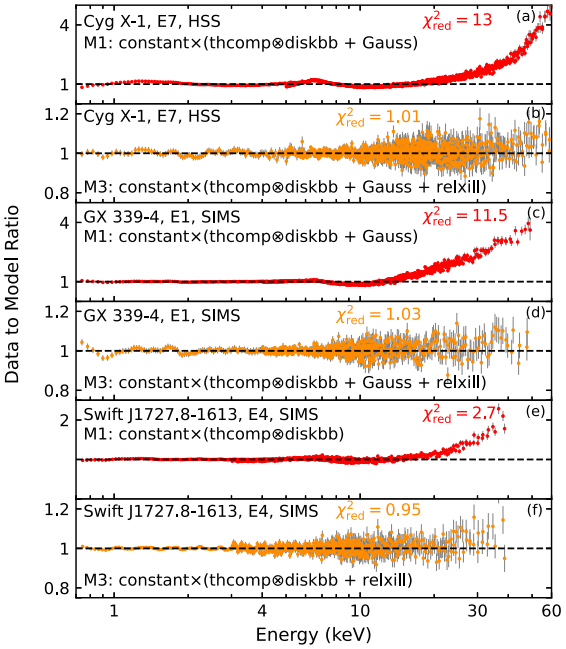

Figure 3. Variation of the data to model ratio of the HSS/HIMS spectra of Cyg X−1, GX 339–4, and *Swift* J1727.8–1613 fitted with model combination M1 and M3. The improvement in the respective fits by incorporating the reflection model component over M1 is depicted in panels (b), (d), and (f). See the text for details.

4.2.3 *Spectral properties*

The spectral energy distribution of the individual sources are generally described by the model combination comprising thermal Comptonization, standard disc, and occasionally reflection components. Although several models developed based on different coronal geometries are found to describe the observed spectra satisfactorily, we examine the spectral states of the respective sources using model M1 and M3 from the extracted spectral parameters. We present the best-fitting and estimated model parameters for each source in Table 3. The variation of the spectral parameters over different

observational epochs indicates the presence of distinct spectral states of the sources under consideration.

We find that the effects of Comptonization are noticeably high during the LHS of Cyg X−1 with covering fraction $cov_{\rm frac} \sim 0.61^{+0.04}_{-0.04} - 0.77^{+0.02}_{-0.02}$, indicating Comptonization of up to ∼ 77 per cent of the soft photons in the LHS spectra. In addition, a high Comptonized flux contribution of 77–80 per cent is also observed in the spectra (see Table 3). Indeed, such a high $cov_{\rm frac}$ results in low photon index ($\Gamma_{\rm th} \lesssim 1.64^{+0.02}_{-0.02}$) as observed during the LHS observations of Cyg X−1. In the HIMS and LHS of *Swift* J1727.8−1613, we find $cov_{\rm frac} \sim 0.35^{+0.01}_{-0.01} - 0.82^{+0.02}_{-0.02}$ and $\Gamma_{\rm th} \sim 1.71^{+0.03}_{-0.02} - 2.11^{+0.05}_{-0.04}$ with up to ∼ 64 per cent Comptonized emission. Similarly, LHS of IGR J17091−3624 which is dominated by the Comptonized emission (∼ 87 per cent flux contribution) yields harder ($\Gamma_{\rm th} \sim 1.62^{+0.02}_{-0.01}$) spectral characteristics. On the other hand, the HSS/SIMS spectra of Cyg X−1 and *Swift* J1727.8−1613 results in low Comptonization with $cov_{\rm frac}$ in the range $0.005^{+0.002}_{-0.002} - 0.38^{+0.04}_{-0.03}$ and thermal disc emission with 39–98 per cent flux contribution along with a steeper spectral index ($\Gamma_{\rm th} \sim 2.32^{+0.06}_{-0.04} - 5.14^{+0.36}_{-0.39}$). Moreover, HSS with 76–98 per cent disc contribution are observed for LMC X−1, 4U 1630−47, LMC X−3, and 4U 1957+115 with negligible Comptonized emission ($cov_{\rm frac} < 0.1$) as shown in Table 3. We find that GX 339−4 (*Swift* J151857.0−572147) exhibits intermediate spectral characteristics with $cov_{\rm frac} \sim 0.34$ (0.21) and $\Gamma_{\rm th} \sim 2$ (2.5) with ∼ 50 per cent (78 per cent) disc emission during SIMS (HSS).

The reflection spectroscopy of Cyg X−1, *Swift* J1727.8–1613, and GX 339–4 with model `M3` during the HSS/SIMS results in disc ionization parameter ($\log \xi$) in the range of $3.31^{+0.05}_{-0.05} - 4.29^{+0.14}_{-0.21}$ erg cm s^{-1}, iron abundance ($A_{\rm fe}$) between $\sim 4.61^{+0.36}_{-0.31}$ and $6.35^{+2.08}_{-1.46}$ $A_\odot$, and reflection fraction ($R_{\rm f}$) ranging $\sim 0.59^{+0.05}_{-0.11}$ to $3.16^{+0.35}_{-0.33}$. Here, $A_\odot$ represents the solar iron abundance. The best-fitting parameters of the `relxill` component obtained from model `M3` are tabulated in Table 4, whereas the parameters associated with other spectral components (`diskbb` and `thcomp`) of `M3` are presented in Table 3 for the respective sources. Notably, a high ionization ($\log \xi \sim 4$) observed in HSS/SIMS generally suggests the reflection of significant coronal emission producing strong reflection signatures.

In addition, we find that the model component `relxilllp` (T. Dauser et al. 2013) also delineates the reflection features assuming the primary source emissivity profile from a lamppost corona. Moreover, another reflection flavor `relxillCp`, in which the spectrum of the coronal emission is computed from the `nthComp` (A. A. Zdziarski, W. N. Johnson & P. Magdziarz 1996) model of spherical geometry, also fits the data for Cyg X−1 (E6 and E7) and *Swift* J1727.8–1613 (E4). Therefore, it is evident that the reflection spectroscopy also results in degeneracy among several models relying on contemporary coronal geometries.

Overall, the wide-band spectro-temporal analysis (see Sections 4.1 and 4.2) confirms the presence of distinct spectral states in BH-XRBs, but falls short of resolving the inherent degeneracy among the possible coronal geometries. This highlights the importance of incorporating X-ray polarimetric observations into the study of BH-XRBs. Subsequently, we explore how polarization measurements offer deeper insights to this issue.

4.3 Polarization measurements

We study the in-depth polarimetric properties of the 11 BH-XRBs observed with *IXPE* during multiple campaigns. In general, the polarization measurements are performed using two distinct methods. The first one relies on the model-independent approach based on the analysis of the polarization cube (F. Kislat et al. 2015) using the

Table 4. Best-fitting parameters of the reflection model component `relxill` used in the model combination `M3: constant×Tbabs×(thcomp⊗diskbb + relxill)`. The parameters of other components in `M3` are listed in Table 3 for the respective epochs. Here, Γ is the power-law index of the source spectrum, $A_{\rm fe}$ is the iron abundance in solar units, $\log \xi$ is the ionization of the accretion disc, and $R_{\rm f}$ is the reflection fraction parameter. $F_{\rm relxill}$ is the flux associated with the `relxill` model component. The references for the spin and inclination of the sources are mentioned in the footnote. See the text for details.

Source	Epoch	Spin (a_*)	Inclination (i) (°)	Γ	$A_{\rm fe}$ ($A_\odot$)	$\log \xi$ (log erg cm s^{-1})	$R_{\rm f}$	$F_{\rm relxill}$ [a] (10^{-8} erg cm^{-2} s^{-1})	Spectral State
Cyg X−1 [b]	E6	0.98 [c]	27 [c]	$2.32^{+0.04}_{-0.06}$	$6.35^{+2.08}_{-1.46}$	$3.86^{+0.09}_{-0.08}$	$0.67^{+0.04}_{-0.04}$	2.33	HSS
	E7	0.98 [c]	27 [c]	$2.04^{+0.01}_{-0.01}$	$4.61^{+0.36}_{-0.31}$	$3.31^{+0.05}_{-0.05}$	$1.11^{+0.03}_{-0.03}$	2.14	HSS
GX 339−4 [d]	E1	0.85 [c]	50 [c]	$2.27^{+0.03}_{-0.03}$	0.5 [e]	$3.92^{+0.12}_{-0.05}$	$3.16^{+0.35}_{-0.33}$	0.54	SIMS
Swift J1727.8–1613 [f]	E4	0.98 [c]	40 [c]	$2.19^{+0.03}_{-0.02}$	5.02 [e]	$4.11^{+0.12}_{-0.13}$	$0.68^{+0.17}_{-0.14}$	5.44	SIMS
	E5	0.98 [c]	40 [c]	$2.48^{+0.02}_{-0.03}$	5.1 [c]	$4.29^{+0.14}_{-0.21}$	$0.59^{+0.05}_{-0.11}$	4.38	SIMS

Note. $A_\odot$ is the solar iron abundance, $r_{\rm g} = GM/c^2$.
[a]Calculated in 1–100 keV energy range.
[b]A. Kushwaha et al. (2021).
[c]Frozen values.
[d]G. Mastroserio et al. (2025).
[e]Fixed to the best-fitting values.
[f]J.-Q. Peng et al. (2024a).

dedicated PYTHON package IXPEOBSSIMV31.0.3[7] (L. Baldini et al. 2022). This provides the polarimetric properties by computing the PD and PA from the normalized Stokes parameters without any prior assumption on the emission mechanism. The alternative method depends on the simultaneous modelling of the I, Q, and U Stokes spectra in XPSEC. In this approach, the source intensity spectrum (I) is modelled using the appropriate physical components responsible for the emission mechanism and a polarization model accounting for the Q and U spectra (T. E. Strohmayer 2017). Accordingly, we carry out both model-independent and model-dependent analyses to ensure the consistency of the polarimetric measurements.

We perform model-independent polarization cube analysis using XPBIN tool inside the software routine with PCUBE algorithm. Following A. Kushwaha et al. (2023) and S. Majumder et al. (2024a, b), we consider all events from the three DUs of *IXPE* in the analysis. Subsequently, the normalized Q and U Stokes parameters, the polarization degree (PD $= \sqrt{(Q/I)^2 + (U/I)^2}$) and polarization angle (PA $= \frac{1}{2}\tan^{-1}(U/Q)$) are computed in 2–8 keV energy band for all observations of the respective sources. Following the guidelines of IAU[8] (G. Contopoulos & A. Jappel 1974), we adopt the convention that PA increases counter-clockwise from North to East direction in the sky. We also calculate the minimum detectable polarization at 99 per cent confidence level (MDP$_{99}$%) and the significance (SIGNIF in units of σ) for each measurement. It may be noted that an observed PD $>$ MDP$_{99}$% indicates a polarization level that would arise from random statistical fluctuations with only 1 per cent chance probability (F. Kislat et al. 2015). All the calculated polarimetric parameters and the measurement statistics are tabulated in Table 5. In Fig. 4, we present 3σ confidence contours associated with the measurements of PD and PA for the respective sources in different spectral states.

We find significant degree of polarized emission (PD $>$ MDP$_{99}$%) in all sources except LMC X−1, *Swift* J151857.0−572147, and MAXI J1744−294. More precisely, we find that PD varies within 1.22 ± 0.35 per cent − 21.41 ± 0.41 per cent including all sources in different spectral states within 2–8 keV energy band. We note that Cyg X−3 shows the maximum degree of polarization, whereas GX 339−4 exhibits the lowest PD ($>$ MDP$_{99}$%) among all sources under consideration. Further, a significant variation of PD is observed over different spectral states of the sources. For example, Cyg X−1 manifests a maximum PD of $\sim$ 4.8 per cent in the LHS, which decreases to $\sim$ 1.4 per cent in the HSS. Interestingly, a similar variation of PD is observed over several spectral states during the outburst phase of *Swift* J1727.8–1613 in which the polarization degree drops down to $\sim$ 0.4 per cent (HSS) from $\sim$ 4.7 per cent (HIMS) and again increases to $\sim$ 3.2 per cent in the LHS. Most astonishingly, 4U 1630–47 exhibits exceedingly high PD in the HSS ($\sim$ 8.3 per cent) and SPL ($\sim$ 6.8 per cent), respectively. Moreover, we find an unprecedentedly high PD of $\sim$ 9 per cent in the LHS of the recent outburst of IGR J17091–3624, which is the maximum reported for any confirmed BH-XRB observed with *IXPE* to date (see also M. Ewing et al. 2025). In contrast, 4U 1957+115 and LMC X−3 are found to show $\sim$ 1.9 per cent and $\sim$2.4 per cent–3 per cent polarization in the HSS, respectively. It may be noted that, for GX 339−4, significant PD ($\sim$ 1.2 per cent, E1) is obtained in 3−8 keV energy range (see also G. Mastroserio et al. 2025), whereas null-detection is seen considering the entire *IXPE* energy band of 2−8 keV. Moreover, we find that PA of the sources in different spectral states shows marginal variation (see Table 5).

Null-detection of polarization: It is worth mentioning that we reconfirm the null-detection of polarized emission (PD $<$ MDP$_{99}$%) for a few sources under consideration. In particular, LMC X−1 remains the first source that fails to manifest significant polarization with *IXPE* (see Table 5 and J. Podgorný et al. 2023). Further, *Swift* J151857.0−572147 exhibits a PD of $\sim$ 0.25 per cent in 2−8 keV which remains significantly low from the corresponding MDP$_{99}$ $\sim$ 0.78 per cent, confirming a null-detection. This finding contradicts the polarization detection with PD $\sim$ 1.3 per cent as reported by S. Mondal et al. (2024). This discrepancy possibly arises as the present analysis is carried out using the latest version of the software IXPEOBSSIMV31.0.3, fixing the bugs related to the visualization of polarization cubes in the previous releases.[9] We emphasize that our results are consistent with the recent polarization measurements of *Swift* J151857.0−572147 (Y.-S. Ling et al. 2024). Further, the null-detection of polarization is also observed in a few observations of *Swift* J1727.8–1613 (E6, E7), GX 339–4 (E2,) and LMC X−3 (E3). In addition, for the first time, we report the null-detection of X-ray polarization with PD ($\sim$ 0.7 per cent) $<$ MDP$_{99}$(1.3 per cent) in the recently discovered BH-XRB candidate MAXI J1744−294 during HSS.

4.4 Energy-dependent polarization

We further explore energy-dependent polarization properties of the selected sources that confirm the presence of significant polarized emission in 2−8 keV energy range of *IXPE*. For each source except 4U 1957+115, IGR J17091−3624, and GX 339–4, we divide 2−8 keV energy range into six linearly spaced energy bins and estimate polarization using the model-independent approach (see also A. Veledina et al. 2023; J. Svoboda et al. 2024a). For 4U 1957+115, IGR J17091−3624, and GX 339–4, only four energy bins are considered for the energy-dependent study to ensure relatively improved photon statistics per energy bin (see also L. Marra et al. 2024). Further, we estimate the significance of the energy variation of PD over these bins following H. Krawczynski et al. (2022) and S. Majumder et al. (2024b). In doing so, we consider PD in 2−8 keV energy range (see Table 5) as the null hypothesis against which the significance of energy variations in PD is computed for each epoch of a given source. With this, following S. Majumder et al. (2024b), we calculate the probability of rejecting the null hypothesis using $(N-1)$ degrees of freedom, taking into account the variation of PD over N energy bins for the respective cases. This essentially indicates the confidence level at which the PD variation is significant over different energy bins. The obtained significance levels of the energy variation of PD are mentioned in Table 5 for the respective cases. We observe that this significance varies from $\lesssim 1\sigma$ to $> 4\sigma$ across different epochs of the sources in various spectral states. In Fig. 5, we present the variation of PD with energy over different observational epochs using filled circles in the respective panels. The histograms in colours represent the MDP$_{99}$% associated with the measurements in the selected energy bins for the corresponding epochs. Note that, for a given source, when multi-epoch observations are available, we present the results for two epochs of different spectral states only, except LMC X−3.

Interestingly, we observe that Cyg X−1 and *Swift* J1727.8−1613 show similar energy variation of PD within $\sim$2 per cent−6 per cent in different spectral states (LHS, HSS, HIMS, and SIMS). Moreover, for

[7] https://ixpeobssim.readthedocs.io/en/latest/

[8] https://aas.org/posts/news/2015/12/iau-calls-consistency-use-polarization-angle

[9] https://ixpeobssim.readthedocs.io/en/latest/release_notes.html

Table 5. Model-independent polarimetric results obtained using the PCUBE algorithm in the 2–8 keV energy band from *IXPE* observations of 11 BH-XRBs. PD and PA represent the polarization degree and angle, respectively. Q/I and U/I are the normalized Stokes parameters. MDP denotes the minimum detectable polarization, and SIGNIF is the detection significance in units of σ. PD_E represents the significance of the energy variation of PD in units of σ. Grey-shaded entries indicate null-detection of polarization. See the text for details.

Source	Epoch	Obs. ID	PD (per cent)	PA (°)	Q/I (per cent)	U/I (per cent)	MDP_{99} (per cent)	SIGNIF (σ)	Spectral State	Remarks	PD_E [a] Sig. (σ)
Cyg X−1	E1	01002901	3.70 ± 0.19	-20.75 ± 1.50	2.77 ± 0.19	-2.45 ± 0.19	0.59	19	LHS	Detection	2.8
	E2	01250101	3.79 ± 0.32	-25.54 ± 2.39	2.38 ± 0.32	-2.95 ± 0.32	0.96	12	LHS	Detection	< 1
	E3	02008201	2.50 ± 0.40	-19.23 ± 4.63	1.95 ± 0.40	-1.55 ± 0.40	1.22	5.7	HSS	Detection	< 1
	E4	02008301	2.46 ± 0.30	-22.89 ± 3.45	1.71 ± 0.30	-1.76 ± 0.30	0.90	8	HSS	Detection	3
	E5	02008401	2.01 ± 0.29	-25.82 ± 4.11	1.25 ± 0.29	-1.58 ± 0.29	0.88	6.6	HSS	Detection	> 4
	E6	02008501	1.44 ± 0.28	-25.38 ± 5.66	0.91 ± 0.28	-1.12 ± 0.28	0.86	4.5	HSS	Detection	1.2
	E7	02008601	2.07 ± 0.23	-36.37 ± 3.19	0.61 ± 0.23	-1.98 ± 0.23	0.70	9	HSS	Detection	1.1
	E8	03002201	3.75 ± 0.47	-24.22 ± 3.61	2.49 ± 0.47	-2.80 ± 0.47	1.43	7.6	LHS	Detection	1.8
	E9	03003101	3.04 ± 0.48	-18.35 ± 4.54	2.44 ± 0.48	-1.82 ± 0.48	1.46	5.9	LHS	Detection	< 1
	E10	03010001	4.65 ± 0.46	-27.77 ± 2.85	2.63 ± 0.46	-3.83 ± 0.46	1.4	10.1	LHS	Detection	< 1
	E11	03010101	4.76 ± 0.53	-32.64 ± 3.18	1.99 ± 0.53	-4.32 ± 0.53	1.60	9	LHS	Detection	1.5
	E12	03002599	2.79 ± 0.19	-21.97 ± 1.97	2.01 ± 0.19	-1.94 ± 0.19	0.58	14.5	HSS	Detection	> 4
4U 1630−47	E1	01250401	8.34 ± 0.17	17.80 ± 0.60	6.79 ± 0.17	4.86 ± 0.17	0.53	48	HSS	Detection	> 4
	E2	02250601	6.77 ± 0.21	21.36 ± 0.90	4.97 ± 0.21	4.59 ± 0.21	0.65	31.7	SPL	Detection	> 4
Cyg X−3	E1	02001899	20.60 ± 0.31	-89.79 ± 0.43	-20.60 ± 0.31	-0.15 ± 0.31	0.94	66.3	LHS	Detection	> 4
	E2	02250301	10.58 ± 0.28	-87.39 ± 0.75	-10.54 ± 0.28	-0.96 ± 0.28	0.85	38	HSS	Detection	> 4
	E3	02009101	21.41 ± 0.41	-88.09 ± 0.55	-21.36 ± 0.41	-1.43 ± 0.41	1.24	52.7	SIMS	Detection	> 4
	E4	03250301	11.98 ± 0.43	-85.22 ± 1.03	-11.82 ± 0.43	-1.99 ± 0.43	1.31	27.8	HSS	Detection	> 4
LMC X−1	E1	02001901	1.04 ± 0.40	53.97 ± 11.09	-0.32 ± 0.40	0.99 ± 0.40	1.23	1.8	HSS	Null-detection	–
4U 1957+115	E1	02006601	1.85 ± 0.37	-42.09 ± 5.75	0.19 ± 0.37	-1.84 ± 0.37	1.13	4.5	HSS	Detection	1.7
LMC X−3	E1	02006599	3.04 ± 0.40	-44.24 ± 3.77	0.08 ± 0.40	-3.04 ± 0.40	1.21	7.2	HSS	Detection	1.8
	E2	03004899	2.39 ± 0.37	-38.43 ± 4.45	0.54 ± 0.37	-2.33 ± 0.37	1.13	6	HSS	Detection	2.3
	E3	03004901	2.19 ± 0.77	-39.42 ± 10.01	0.42 ± 0.77	-2.15 ± 0.77	2.32	2.4	HSS	Null-detection	–
	E4	03005001	2.84 ± 0.52	-47.32 ± 5.24	-0.23 ± 0.52	-2.83 ± 0.52	1.57	5	HSS	Detection	< 1
Swift J1727.8−1613	E1	02250901	4.72 ± 0.28	2.50 ± 1.69	4.71 ± 0.28	0.41 ± 0.28	0.84	17	HIMS	Detection	< 1
	E2	02251001	4.48 ± 0.20	2.28 ± 1.31	4.46 ± 0.20	0.36 ± 0.20	0.62	22	HIMS	Detection	2.8
	E3	02251101	4.39 ± 0.29	0.95 ± 1.87	4.38 ± 0.29	0.15 ± 0.29	0.87	15.3	HIMS	Detection	2.6
	E4	02251201	3.81 ± 0.29	-0.49 ± 2.22	3.81 ± 0.29	-0.07 ± 0.29	0.89	12.8	SIMS	Detection	1.1
	E5	02251301	3.35 ± 0.32	-2.01 ± 2.75	3.34 ± 0.32	-0.23 ± 0.32	0.98	10.4	SIMS	Detection	2.5
	E6	03005701	1.18 ± 0.44	-2.74 ± 10.55	1.18 ± 0.44	-0.11 ± 0.44	1.32	2	HSS	Null-detection	–
	E7	03006001	0.40 ± 0.36	6.05 ± 25.83	0.39 ± 0.36	0.08 ± 0.36	1.08	< 1	HSS	Null-detection	–
	E8	03005801	3.22 ± 0.60	4.18 ± 5.37	3.19 ± 0.60	0.47 ± 0.60	1.83	4.8	LHS	Detection	1.6
GX 339–4	E1 [b]	03005101	1.22 ± 0.35	-71.03 ± 8.17	-0.96 ± 0.35	-0.75 ± 0.35	1.05	3.1	SIMS	Detection	3.3
	E2	03005301	0.47 ± 0.36	-25.15 ± 22.07	0.30 ± 0.36	-0.36 ± 0.36	1.09	0.8	HSS	Null-detection	–
Swift J151857.0–572147	E1	03250201	0.25 ± 0.26	-22.35 ± 29.98	0.17 ± 0.26	-0.17 ± 0.26	0.78	0.5	HSS	Null-detection	–
IGR J17091–3624	E1	04250201	9 ± 1.41	83.71 ± 4.48	-8.78 ± 1.41	1.96 ± 1.41	4.27	6.1	LHS	Detection	1.2
MAXI J1744–294	E1	04250301	0.71 ± 0.42	-15.37 ± 17.21	-0.60 ± 0.42	-0.36 ± 0.42	1.27	1.2	HSS	Null-Detection	–

[a] Computed considering six linear energy bins for all sources except GX 339–4, 4U 1957+115 and IGR J17091–3624, where four linear bins are used.
[b] Measurements in 3–8 keV. Null-detection in 2–8 keV.

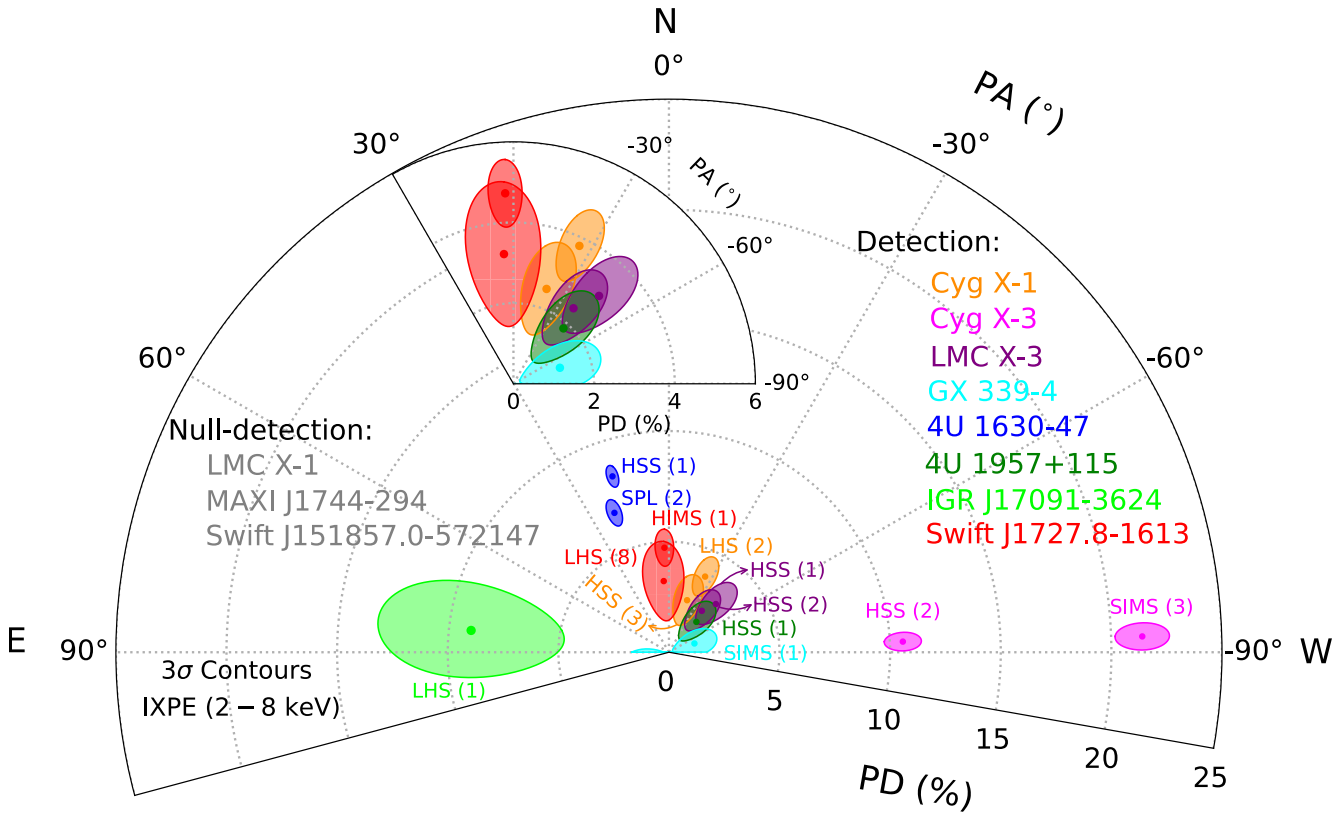

Figure 4. Confidence contours (3σ) in the PD–PA plane obtained from the model-independent polarization measurements using 2–8 keV *IXPE* data, combining all DUs across various spectral states of the sources. The epoch of each observation is indicated in parentheses next to the corresponding spectral state. For *Swift* J151857.0−572147, LMC X−1, and MAXI J1744−294, null-detection of polarization is observed, whereas all other sources exhibit significant polarization. Inset highlights a zoomed-in region of PD–PA space for better clarity.

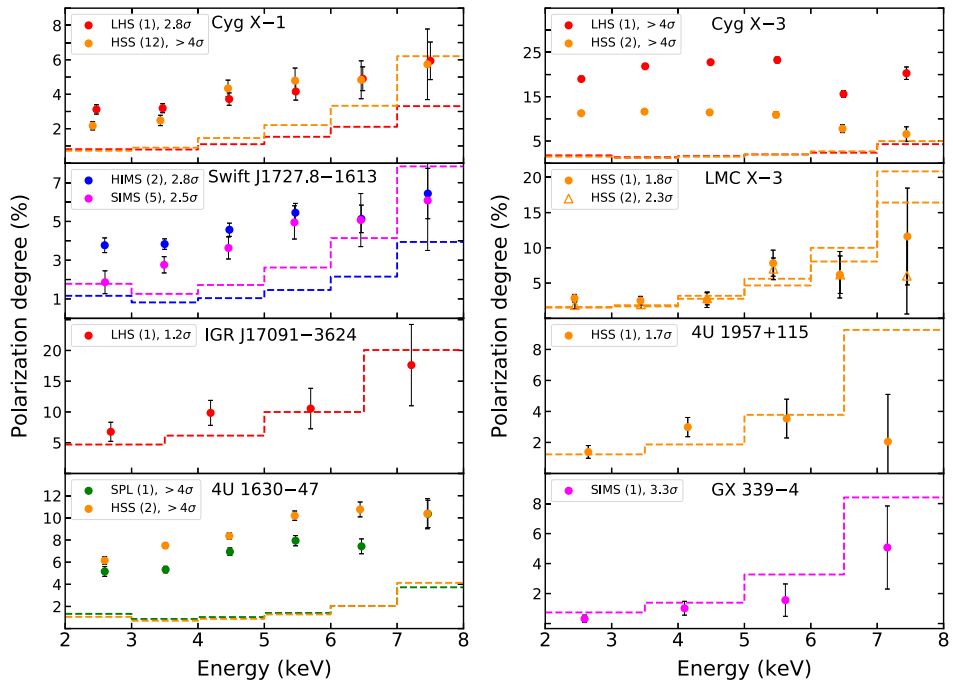

Figure 5. Variation of polarization degree (PD) with energy. In each panel, source name and spectral state (observed during different epoch) are marked. The significance of energy variation of PD for the respective cases are mentioned in units of σ in the plot legends. The histograms represent the minimum detectable polarization at 99 per cent confidence (MDP_{99}%). See the text for details.

Cyg X−1, the variation in PD with energy remains most significant at a confidence level exceeding 4σ in HSS, whereas it remains 2.8σ for *Swift* J1727.8–1613 in HIMS, when all observational epochs are considered (see Fig. 5). Note that, PD $<$ MDP$_{99}$% at higher energy bins in a few epochs of several sources, indicates a null-detection. Interestingly, unlike Cyg X−1 and *Swift* J1727.8–1613, a weak energy dependency of PD is noticed for IGR 17091−3624 in the LHS, for which PD corresponding to two out of four energy bins remain below the MDP$_{99}$% (see Fig. 5). We find a significant increase in PD with energy up to $\sim$ 11 per cent in HSS ($> 4\sigma$) and SPL ($> 4\sigma$) state of 4U 1630−47 (see Fig. 5). Similarly, distinct variations of PD over several energy bins are observed for Cyg X−3 during LHS ($> 4\sigma$) and SIMS ($> 4\sigma$). LMC X−3 shows constant polarization over the initial three energy bins with a sudden jump in PD up to $\sim$ 7.8 per cent at $\sim$ 5.4 keV in both epochs (see Fig. 5). Further, we only observe a marginal variation (1.7σ) of PD in 4U 1957+115 up to $\sim$ 3 per cent. Interestingly, significant (3.3σ) energy variation of polarization degree is observed for GX 339–4. Although, PD $<$ MDP$_{99}$% is obtained in all four energy bins (see Fig. 5). Overall, we state that a significant ($> 3\sigma$) variation of polarization degree with energy is observed only for Cyg X−1, 4U 1630−47, and Cyg X−3, whereas a moderate (2σ to 3σ) variation is seen for *Swift* J1727.8−1613 and LMC X−3. It is worth mentioning that the energy variation of PA for all sources under consideration remains statistically insignificant ($< 2\sigma$). However, we note that PA drops from -30° to -60° at $\sim$ 6 keV in 4U 1957+115, which is marginally significant at 1.6σ confidence level.

4.5 Spectro-polarimetric modelling

We explore the model-dependent spectro-polarimetric properties of the sources from the simultaneous fitting of the *I*, *Q*, and *U* Stokes spectra of *IXPE* in 2–8 keV energy range. Due to the calibration issues (H. Krawczynski et al. 2022; J. F. Steiner et al. 2024; A. Veledina et al. 2024a), only DU1 data are considered for the spectro-polarimetric study of Cyg X−1, Cyg X−3, and *Swift* J1727.8−1613, whereas data combining all the DUs are used for the remaining sources. For simplicity, we first adopt the model combination `M4 : Tbabs×polconst×(diskbb + powerlaw)` for the spectro-polarimetric fitting. Here, `polconst` represents a constant polarization model, where the degree and angle of polarization are treated as the model parameters. The best-fitting results yield $\chi^2_{\rm red}$ ranging from 0.91–1.79 across all selected sources, with PD varying as $\sim$1.16 per cent–13.06 per cent and PA spanning from -89.13° to 85.15°. Note that the spectro-polarimetric modelling of *Swift* J1727.8–1613 does not constrain hydrogen column density, likely due to low-energy threshold of *IXPE* ($\sim$ 2 keV; see A. Veledina et al. 2023; A. Ingram et al. 2024).

Next, we investigate the energy-dependent polarization properties using model-dependent approach for all the sources that demonstrate the signature of X-ray polarization. In doing so, we replace the `polconst` component with the energy-dependent polarization model `polpow`. Empirically, `polpow` assumes a power-law variation in the polarization parameters of the form PD(E) $= A_{\rm norm} \times E^{-A_{\rm index}}$ (in fraction) and PA(E) $= \psi_{\rm norm} \times E^{-\psi_{\rm index}}$ (in $^\circ$) while modelling the *Q* and *U* Stokes spectra. We find that the best-fitting $\psi_{\rm index}$ remains consistent with zero within its 1σ errors and hence, we freeze it to zero during the spectral fitting of all observations. Accordingly, we obtain the best spectral fit for all sources with $\chi^2_{\rm red} \sim 0.97 - 1.46$. Furthermore, integrating PD(E) in 2–8 keV energy range using the best-fitting model parameters ($A_{\rm index}$ and $A_{\rm norm}$), we obtain PD as 3.23 per cent–14.33 per cent. Moreover, with $\psi_{\rm index}$ frozen to zero, the polarization angles are obtained as the best-fitting $\psi_{\rm norm}$ values that vary from -88.92° to 85.11°. Note that, in a few observations of Cyg X−1, 4U 1957+115, and GX 339–4 (see Table 6), the data are unable to constrain the parameters of `polpow` component even at 1σ level, and hence, we refrain from the modelling with `polpow` for these observations. In Table 6, we present the best-fitting model parameters obtained from the spectro-polarimetric study of all sources. We find that the model-dependent polarimetric results are in agreement with the findings of the model-independent study except Cyg X−3, confirming the robustness of the polarization measurements for the individual sources. However, for Cyg X−3, we obtain significantly low PD compared to the results of the model-independent study, likely due to multiple low-energy unpolarized emission lines including strong iron complex around $\sim$ 6.4 keV (A. Veledina et al. 2024a), dominating Stokes spectra.

4.6 Spectro-polarimetric correlation

We examine the spectro-polarimetric correlation properties for each source based on the results obtained from wide-band spectral modelling using model `M1` (see Section 4.2) and the polarimetric measurements (see Section 4.3). Specifically, we explore the correlation between the observed PD obtained from model-independent study, and best-fitting spectral parameters, namely the ratio of disc to Comptonized spectral flux ($F_{\rm ratio}$) in 1–100 keV energy range, and the covering fraction ($cov_{\rm frac}$) obtained from the `thcomp` model. In Fig. 6, we present the variation of PD with $F_{\rm ratio}$ (see Table 3) using different markers, where the covering fraction ($cov_{\rm frac}$, in per cent) is represented by the colours of respective markers. The colour bar on the right indicates the range of $cov_{\rm frac}$. The spectral state and the corresponding epoch (in parentheses) for each observation are marked in the figure.

We observe an apparent anticorrelation between PD and $F_{\rm ratio}$, and a correlation between PD and $cov_{\rm frac}$ for the sources under consideration. However, 4U 1630−47, Cyg X−3, and IGR J17091−3624 deviate significantly from this trend in the PD−$F_{\rm ratio}$ plane (see Fig. 6) and therefore, these sources are excluded from the present correlation study. To ascertain the firmness of the apparent correlations, we compute the Pearson correlation coefficient (ρ) based on the variations in spectro-polarimetric parameters. Excluding the aforementioned outliers, we find $\rho = 0.7$ for the PD−$cov_{\rm frac}$ correlation and $\rho = -0.5$ for the PD−$F_{\rm ratio}$ anticorrelation. Furthermore, excluding epoch E1 of LMC X−3, which appears as a marginal outlier in the PD−$F_{\rm ratio}$ plane, along with 4U 1630−47, Cyg X−3, and IGR J17091−3624 as before, the correlations become relatively stronger yielding $\rho = 0.8$ and $\rho = -0.6$ for PD−$cov_{\rm frac}$ and PD−$F_{\rm ratio}$, respectively.

Furthermore, we find a strong correlation (anticorrelation) between PD and $cov_{\rm frac}$ ($F_{\rm ratio}$) with $\rho \sim 0.9$ (-0.9) for *Swift* J1727.8–1613. In particular, a sharp drop in PD is noticed from $\sim$ 4.7 per cent (HIMS) to $\sim$ 0.4 per cent (HSS) (see also J. Svoboda et al. 2024b) during which $F_{\rm ratio}$ increases from $\sim$ 0.7 to $\sim$ 66 and $cov_{\rm frac}$ noticeably reduces down to 13 per cent from a maximum value of 82 per cent. A similar trend is observed for Cyg X−1 with $\rho = 0.9$ (-0.9) for the respective positive (negative) correlations between PD and $cov_{\rm frac}$ ($F_{\rm ratio}$). As before, a low (high) $F_{\rm ratio} \sim 0.3$ (11.5) and high (low) $cov_{\rm frac}$ $\sim$61 per cent−77 per cent (0.5 per cent−31 per cent) are observed in the LHS (HSS) of Cyg X−1 with PD $\sim$3.7 per cent−4.8 per cent (1.4 per cent−2.1 per cent) (see Fig. 6). Moreover, we also find a similar behaviour in the LHS of IGR J17091–3624, for which a very high PD ($\sim$ 9 per cent) is seen with $cov_{\rm frac} \sim 87$ per cent and $F_{\rm ratio} \sim 0.2$. These findings suggest that a significant contribution in the polarization degree comes from the

Table 6. Results from the spectro-polarimetric modelling of *IXPE* Stokes spectra across different observation epochs of the sources in 2–8 keV energy band. The parameters, with their standard definitions, are obtained from the constant polarization model (`polconst`) and the energy-dependent polarization model (`polpow`). See the text for details.

Source	Epoch	$A_{\rm norm}$	$A_{\rm index}$	$\psi_{\rm norm}$ (°)	$\chi^2_{\rm red}$ (polpow)	$\rm PD_{polpow}$ (per cent)	$\rm PA_{polpow}$ (°)	$\rm PD_{polconst}$ (per cent)	$\rm PA_{polconst}$ (°)	$\chi^2_{\rm red}$ (polconst)
Cyg X−1 [a]	E1	$0.020^{+0.008}_{-0.006}$	-0.43 ± 0.25	-19.83 ± 2.22	1.01	3.93 ± 0.95	-19.83 ± 2.22	3.40 ± 0.26	-19.73 ± 2.24	0.91
	E2	–	–	–	–	–	–	3.41 ± 0.44	-25.13 ± 3.73	1.09
	E3	–	–	–	–	–	–	2.24 ± 0.61	-11.87 ± 7.95	1.15
	E4	$0.008^{+0.005}_{-0.004}$	-0.90 ± 0.56	-17.74 ± 5.45	1.13	3.39 ± 0.40	-17.74 ± 5.45	2.29 ± 0.45	-18.33 ± 5.68	1.13
	E5	$0.003^{+0.003}_{-0.002}$	-1.57 ± 0.57	-8.63 ± 6.16	1.10	3.95 ± 0.31	-8.63 ± 6.16	1.91 ± 0.47	-9.48 ± 7.18	1.10
	E6	0.003 ± 0.002	-1.52 ± 0.68	-16.26 ± 5.74	1.12	3.63 ± 0.47	-16.26 ± 5.74	2.06 ± 0.45	-16.64 ± 6.27	1.13
	E7	0.009 ± 0.005	-0.80 ± 0.47	-25.03 ± 4.56	1.11	3.23 ± 0.99	-25.03 ± 4.56	2.19 ± 0.37	-25.77 ± 4.69	1.11
	E8 [b]	–	–	–	–	–	–	3.04 ± 0.66	-27.09 ± 6.24	1.07
	E9 [b]	–	–	–	–	–	–	3.35 ± 0.67	-25.73 ± 5.79	1.25
	E10 [b]	–	–	–	–	–	–	5.83 ± 0.64	-32.72 ± 3.15	0.96
	E11 [b]	–	–	–	–	–	–	4 ± 0.7	-34.98 ± 5.27	1.05
	E12	$0.009^{+0.005}_{-0.004}$	$-0.9^{+0.4}_{-0.4}$	-24.1 ± 3.26	1.03	3.38 ± 0.48	-24.1 ± 3.26	2.52 ± 0.48	-23.03 ± 3.34	1.05
4U 1630−47	E1 [c]	0.028 ± 0.003	-0.75 ± 0.07	17.90 ± 0.52	1.28	9.25 ± 0.02	17.90 ± 0.52	7.89 ± 0.14	17.94 ± 0.53	1.36
	E2	0.022 ± 0.004	-0.74 ± 0.11	21.45 ± 0.77	1.13	8.02 ± 0.02	21.45 ± 0.77	6.27 ± 0.17	21.30 ± 0.78	1.17
Cyg X−3 [a]	E1 [c]	0.028 ± 0.004	-0.73 ± 0.09	-88.92 ± 0.93	1.46	8.89 ± 0.11	-88.92 ± 0.93	7.09 ± 0.24	-89.13 ± 0.95	1.79
	E2 [c]	0.018 ± 0.002	-0.58 ± 0.11	-88.48 ± 0.97	1.31	4.43 ± 0.16	-88.48 ± 0.97	3.58 ± 0.21	-88.58 ± 1.01	1.36
	E3 [c]	0.024 ± 0.005	-0.87 ± 0.12	-86.98 ± 3.45	1.32	9.75 ± 0.21	-86.98 ± 3.45	7.33 ± 0.31	-87.84 ± 1.19	1.63
	E4 [c]	0.11 ± 0.03	-0.17 ± 0.11	-86.35 ± 1.34	1.31	14.33 ± 0.44	-86.35 ± 1.34	13.06 ± 1.01	-86.29 ± 2.19	1.31
4U 1957+115	E1	–	–	–	–	–	–	1.83 ± 0.33	-43.73 ± 5.19	1.09
LMC X−3	E1	$0.011^{+0.007}_{-0.006}$	-0.82 ± 0.5	-44.29 ± 3.59	1.12	4.08 ± 0.26	-44.29 ± 3.59	2.94 ± 0.37	-44.94 ± 3.63	1.12
	E2	$0.003^{+0.002}_{-0.001}$	-1.67 ± 0.51	-40.47 ± 4.02	1.07	4.71 ± 0.58	-40.47 ± 4.02	2.24 ± 0.56	-38.21 ± 7.17	1.08
	E4	–	–	–	–	–	–	2.85 ± 0.83	-44.18 ± 8.08	1.03
Swift J1727.8−1613 [a]	E1	$0.022^{+0.015}_{-0.009}$	-0.42 ± 0.36	2.21 ± 2.74	1.08	4.26 ± 0.21	2.21 ± 2.74	3.94 ± 0.38	2.02 ± 2.75	1.08
	E2	$0.018^{+0.008}_{-0.006}$	-0.55 ± 0.26	1.53 ± 2.08	1.38	4.29 ± 0.85	1.53 ± 2.08	3.85 ± 0.28	1.41 ± 2.10	1.39
	E3	$0.021^{+0.018}_{-0.010}$	-0.37 ± 0.23	-3.55 ± 3.24	1.04	3.75 ± 0.88	-3.55 ± 3.24	3.53 ± 0.39	-3.63 ± 3.25	1.04
	E4	$0.007^{+0.005}_{-0.004}$	-1.08 ± 0.54	-1.21 ± 3.76	1.05	4.00 ± 0.36	-1.21 ± 3.76	3.11 ± 0.41	–[d]	1.06
	E5	$0.004^{+0.003}_{-0.002}$	-1.49 ± 0.54	-7.21 ± 4.11	0.97	4.59 ± 0.41	-7.21 ± 4.11	2.94 ± 0.45	-8.38 ± 4.44	0.98
	E8	$0.006^{+0.005}_{-0.003}$	-1.28 ± 0.47	0.76 ± 4.21	0.97	4.81 ± 0.17	0.76 ± 4.21	3.22 ± 0.51	2.68 ± 4.54	0.97
GX 339–4 [e]	E1	–	–	–	–	–	–	1.16 ± 0.31	-72.52 ± 7.78	1.03
IGR J17091–3624 [b]	E1	$0.025^{+0.016}_{-0.013}$	-0.89 ± 0.43	85.11 ± 3.88	1.04	10.41 ± 0.51	85.11 ± 3.88	8.24 ± 1.16	85.15 ± 4.03	1.05

[a] Only *IXPE* spectra of DU1 is fitted.
[b] `diskbb` is not required.
[c] `powerlaw` is not required.
[d] Not constrained.
[e] Spectral fitting performed within 3–8 keV range.

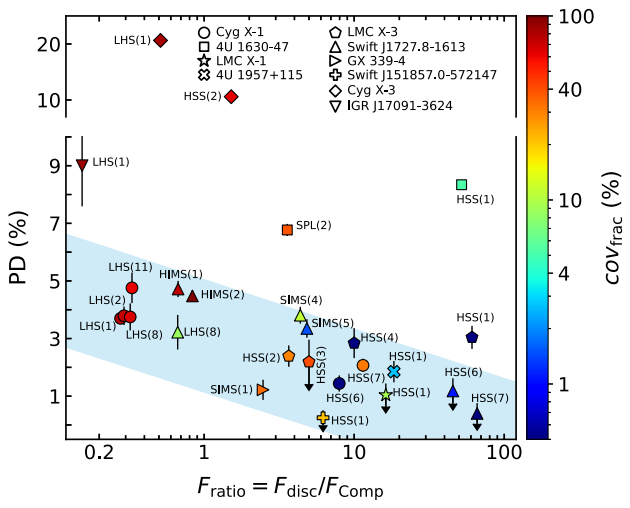

Figure 6. Variation of PD (2–8 keV), obtained from model-independent analysis, as a function of the disc-to-Comptonized flux ratio (F_{ratio}) derived in 1–100 keV energy range from the wide-band spectral modelling. The colour bar represents the covering fraction (cov_{frac}) obtained from `thcomp` model, while each data point is labelled with the corresponding spectral state and observational epoch. Data points within the shaded region (light blue) are used to compute the Pearson correlation coefficient. Downward arrows indicate null-detections of polarization for the respective sources.

Comptonized emission for *Swift* J1727.8–1613, Cyg X−1, and IGR J17091–3624 in the HIMS and/or LHS. Furthermore, we notice a low polarization degree (PD $\lesssim 2$ per cent) for all the sources except 4U 1630−47 and LMC X−3 in the HSS/SIMS with $F_{ratio} \gtrsim 2$ and $cov_{frac} \lesssim 30$ per cent. Interestingly, 4U 1630−47 being the source of extreme soft nature ($F_{ratio} \sim 52$, $cov_{frac} \sim 5$ per cent) manifests a high polarization degree of ~ 8.3 per cent in the HSS, whereas it reduces to 6.8 per cent in the SPL state with $F_{ratio} \sim 3.6$ and $cov_{frac} \sim 38$ per cent. We observe that 4U 1957+115 (GX 339–4) shows PD ~ 1.2 per cent (1.9 per cent) with $cov_{frac} \sim 2.7$ per cent (34 per cent) and $F_{ratio} \sim 18$ (2.4) in the HSS (SIMS). Moreover, LMC X−3 exhibits moderate polarization with PD in the range of 2.4 per cent–3 per cent for $F_{ratio} \gtrsim 4$ and $cov_{frac} \sim 0.5$ per cent during the HSS.

5 DISCUSSION

In this study, we present a comprehensive spectro-polarimetric investigation of 11 BH-XRBs using quasi-simultaneous observations from *IXPE*, *NICER*, *AstroSat,* and *NuSTAR*. *IXPE* data are analysed to examine the polarization properties in 2–8 keV energy range, while combined *NICER*, *AstroSat*, and *NuSTAR* observations provide insights into the spectro-temporal behaviour across the wide energy range (0.5–100 keV). Subsequently, the spectro-polarimetric findings are used to investigate the accretion-ejection dynamics and geometry surrounding the sources.

5.1 Spectro-temporal properties and spectral states

Spectro-temporal studies using *NICER*, *NuSTAR*, and *AstroSat* observations in 0.5–100 keV energy range impart distinct variability properties in various spectral states of the sources (see Sections 4.1 and 4.2). The obtained results are in line with the spectro-temporal characteristics generally seen in the respective spectral states of BH-XRBs (T. Belloni et al. 2005; J. E. McClintock et al. 2009; A. Nandi et al. 2012; H. Sreehari et al. 2019b; M. Méndez et al. 2022; U. Aneesha et al. 2024). These findings reinforce the presence of distinct spectral states as observed during the multimission campaigns of the sources.

In particular, we observe a high fractional variability amplitude $rms_{tot}\% \sim 30 - 52$ in the PDS of LHS, whereas significantly low variability with $rms_{tot}\% \sim 6 - 14$ are seen in the intermediate states (HIMS and SIMS) of the sources (see Table 3). Negligible power distribution at lower frequencies results in marginal variability ($rms_{tot}\% \sim 1 - 10$) for the sources in the HSS (see Table 3 and Fig. 2). In addition, we find the presence of a strong type-C QPO feature at ~ 1.4 Hz (E1), which evolves to ~ 6.7 Hz (E2–E5), during the HIMS and SIMS of *Swift* J1727.8−1613 over a wide energy range of 0.5–100 keV with *NICER*, *NuSTAR*, and *AstroSat* observations (see Fig. 2). The origin of this QPO is attributed to a strong Comptonizing corona surrounding the central source (S. Chakrabarti & L. G. Titarchuk 1995; S. K. Chakrabarti et al. 2008; A. Nandi et al. 2024); however, based on the correlation between the evolution of QPO frequency and quasi-simultaneous radio jet ejections, J. Liao et al. (2024) suggest a jet-like, vertically elongated corona for *Swift* J1727.8–1613. A similar type-C QPO at ~ 0.2 Hz is detected in LHS of IGR J17091–3624 (see Fig. 2). Moreover, we also observe a type-B QPO in the disc-dominated SIMS of GX 339–4 in the 0.5–80 keV energy range from *NICER* and *AstroSat* data. Similar type-B QPOs have been observed earlier in GX 339–4, indicating the presence of a compact corona located very close to the black hole, accompanied by dominant disc emission (A. Nandi et al. 2012; U. Aneesha et al. 2024).

The wide-band (0.7–60 keV) energy spectral analysis reveals distinct spectral states of each source. The observed spectra of all sources are well described by a standard accretion disc component (`diskbb`) combined with thermal Comptonization of soft photons by a spherical corona (`thcomp`) (see Table 3 and Fig. 2). The spectral properties exhibit a strong correlation with the spectral states of the sources. In particular, during LHS and HIMS, the spectra are dominated by Comptonized emission, contributing ∼64 per cent–87 per cent of the total flux, accompanied by a high covering fraction ($cov_{frac} \sim 61 - 87$). In contrast, the HSS and SIMS are characterized by a prominent disc component, contributing up to 39 per cent–98 per cent with marginal Comptonization effects (cov_{frac} ∼0.5 per cent–38 per cent) across all sources. We observe the present findings to be broadly consistent with the previously reported results for the respective sources. For example, J. Svoboda et al. 2024b found a steeper $\Gamma_{th} \sim 4.9$ and low $cov_{frac} \sim 20$ per cent in the HSS of *Swift* J1727.8–1613, which agrees well with our findings of $\Gamma_{th} \sim 4.6 - 5.1$ and $cov_{frac} \sim 17$ per cent. In addition, the LHS results for Cyg X−1 (E1) are consistent with those of H. Krawczynski et al. (2022), except for their measurement of a high electron temperature, which is likely because of the differences in spectral energy coverage and/or the choice of model components.

We also notice that the Comptonization model with a disc-like coronal geometry (`comptt`) yields a comparable fit to the observed spectra similar to the spherical corona model (`thcomp`). This evidently indicates the degeneracy in determining the corona geometry (see Section 4.2). Furthermore, strong reflection signatures detected in the soft state observations (HSS and SIMS) of Cyg X−1, *Swift* J1727.8–1613, and GX 339–4 allow the detailed investigation of alternative coronal geometries using various reflection models (see Section 4.2). We also observe that the reflected emission, either from a lamppost corona, modelled with `relxilllp`, or from a spherical corona as described in `relxillCp`, can be reproduced

satisfactorily considering a highly ionized accretion disc ($\log \xi \sim 4$). All these findings highlight the inherent degeneracy among different disc–corona geometry models in explaining the observed spectral characteristics.

5.2 Model prescriptions and limitations of X-ray polarization in BH-XRBs

X-ray polarization measurements with *IXPE* reveal significant polarized emission across several spectral states of the sources in 2–8 keV energy range, except for LMC X−1 (see Section 4.3 and J. Podgorný et al. 2023), *Swift* J151857.0−57214 (see Section 4.3 and Y.-S. Ling et al. 2024) and MAXI J1744−294 (see Section 4.3). We find that Cyg X−1 exhibits PD within 3 per cent–4.8 per cent in LHS, which decreases to 1.4 per cent–2.5 per cent in HSS. A similar noticeable reduction in the PD from 4.7 per cent (HIMS) to 0.4 per cent (HSS) is also observed for the exceptionally bright transient *Swift* J1727.8−1613. The most recent *IXPE* observation of this source confirms the recovery of PD $\sim$ 3.2 per cent in the faint LHS. We mention that these results are in agreement with the previously reported polarimetric findings of Cyg X−1 (H. Krawczynski et al. 2022; A. Jana & H.-K. Chang 2024; J. F. Steiner et al. 2024) and *Swift* J1727.8−1613 (A. Veledina et al. 2023; A. Ingram et al. 2024; J. Podgorný et al. 2024; J. Svoboda et al. 2024b).

Intriguingly, an exceptionally high PD of $\sim$ 8.3 per cent is observed in the HSS of 4U 1630−47, which drops to $\sim$ 6.8 per cent during the SPL state exhibiting strong ($> 4\sigma$) energy dependency (see Table 5 and Fig. 5; also A. Kushwaha et al. 2023; N. Rodriguez Cavero et al. 2023; D. Rawat et al. 2023b, a; A. Ratheesh et al. 2024). In contrast, low PD values are observed in several sources: LMC X−3 ($\sim$2.4 per cent–3 per cent), 4U 1957+115 ($\sim$ 1.9 per cent), and GX 339–4 ($\sim$ 1.2 per cent), being consistent with the previous measurements (A. Garg, D. Rawat & M. Méndez 2024; L. Marra et al. 2024; S. Majumder et al. 2024a; J. Svoboda et al. 2024a; G. Mastroserio et al. 2025). In this work, we report polarization detections analysing the most recent *IXPE* observations of Cyg X−3 (PD $\sim$ 21.4 per cent, SIMS), LMC X−3 (PD $\sim$ 2.4 per cent, HSS), and IGR J17091−3624 (PD $\sim$ 9 per cent, LHS), apart from the earlier measurements of these sources. In addition, for the first time to the best of our knowledge, we report the null-detection of X-ray polarization in LMC X−3 (E3) and a newly discovered BH-XRB candidate MAXI J1744–294. We note that, subsequent to our report, null-detection of polarization for MAXI J1744−294 is also confirmed by L. Marra et al. (2025).

Meanwhile, several models have been proposed to account for the observed polarization in BH-XRBs. For instance, remarkably high PD ($\sim$ 8.3 per cent) of 4U 1630−47 is attributed to the emission from a partially ionized thin/slim accretion disc viewed at inclination $i \gtrsim 60^\circ$ (A. Ratheesh et al. 2024). Similar explanation is also suggested for LMC X−3 in the HSS that exhibits PD $\sim$ 3 per cent at $i \sim 70^\circ$ (S. Majumder et al. 2024a; J. Svoboda et al. 2024a). Further, scattering of photons in strong disc winds of different opening angles ($\alpha_w \sim 30^\circ - 40^\circ$) has also been suggested as another possible mechanism to explain high PD values of 4U 1630−47 (A. Kushwaha et al. 2023; D. Rawat et al. 2023b; A. P. Nitindala, A. Veledina & J. Poutanen 2025). However, R. Tomaru, C. Done & H. Odaka (2024) demonstrated that electron scattering in an optically thin wind produces polarization in a direction opposite to that obtained from the intrinsic emission from an optically thick disc. As a result, the wind component is expected to depolarize the total emission, including the intrinsic disc emission. Therefore, the presence of disc–wind from the optically thick disc appears to be insufficient to account for the observed high PD in 4U 1630−47. On the other hand, in high-spin black hole systems, strong relativistic effects cause intense gravitational lensing that bends emitted photons back on to the disc. This enhances the reflection features and significantly affects the observed polarization (see Section 4.2; J. D. Schnittman & J. H. Krolik 2009). Such an effect appears consistent with the polarimetric observations (PD $\sim$1.2 per cent–2.5 per cent) in the soft state as reported for rapidly spinning systems like Cyg X−1 ($a_* > 0.998$) and 4U 1957 + 115 ($a_* \sim 0.988$) (L. Marra et al. 2024; J. F. Steiner et al. 2024).

Furthermore, it has been suggested that $\sim$ 4 per cent (Cyg X−1, LHS) and $\sim$ 9 per cent (IGR J17091−3624, LHS) polarization can be obtained from a wedge-shaped corona with mildly relativistic outflowing plasma model of A. M. Beloborodov (1998) having inclination in the range $30^\circ \lesssim i \lesssim 60^\circ$ (J. Poutanen et al. 2023; M. Ewing et al. 2025). A similar model of bulk Comptonization involving a mildly relativistic outflow predicts an even higher polarization degree up to $\lesssim$ 10 per cent (J. Dexter & M. C. Begelman 2024). Notably, observed $\sim$ 4.7 per cent PD at $i \sim 40^\circ$ in HIMS of *Swift* J1727.8–1613 also seems to be consistent with the predictions from a wedge-shaped corona with outflowing plasma velocity $\lesssim 0.2c$ (J. Poutanen et al. 2023). However, QPOs are detected in *Swift* J1727.8–1613 (0.5–100 keV) and IGR J17091−3624 (3−79 keV) during observations simultaneous with *IXPE*, although their physical origin remains unclear within the framework of the outflowing corona geometry. On the other hand, N. Kumar (2024) predicted PD $\sim$0.5 per cent−4 per cent assuming a simple static spherical corona for $30^\circ \lesssim i \lesssim 60^\circ$. This appears broadly consistent with the low PD of $\sim$ 1.2 per cent observed at $i \sim 30^\circ$ in the SIMS of GX 339–4.

All the above interpretations of the polarimetric findings point towards a persistent degeneracy in understanding the different accretion-ejection dynamics. More precisely, predictions regarding the disc–corona–jet geometry become even more challenging when the simultaneous origin of temporal features (QPOs), spectral distributions and polarization (PD) is considered. This emphasizes the need for a unified framework of accretion-ejection processes in BH-XRBs that can consistently explain both timing and spectro-polarimetric observations.

5.3 Accretion-ejection scenarios in BH-XRBs

Following the discussion of model degeneracies and the need for a unified model framework, we next explore physically motivated accretion–ejection geometries capable of explaining the commonly observed spectro-temporal features, while also offering a promising basis for interpreting the spectro-polarimetric signatures in BH-XRBs. Towards this, a plausible disc–corona–jet configuration based on the two-component accretion flow model (S. Chakrabarti & L. G. Titarchuk 1995; S. K. Chakrabarti 1996) is illustrated in Fig. 7. In this model, the accretion flow around black holes comprise with Keplerian disc flanked between the sub-Keplerian components. This sub-Keplerian component generally forms the post-shock corona (PSC, equivalently Comptonizing corona) in the inner region of the disc (S. Chakrabarti & L. G. Titarchuk 1995; D. Molteni et al. 1996; S. K. Chakrabarti et al. 2008; A. Nandi et al. 2012; S. Das et al. 2014). Soft photons from the Keplerian disc are upscattered by hot electrons present in the corona and produce the hard spectral tail seen in BH-XRBs. The inner edge of the Keplerian disc smoothly connects to the outer boundary of the coronal region.

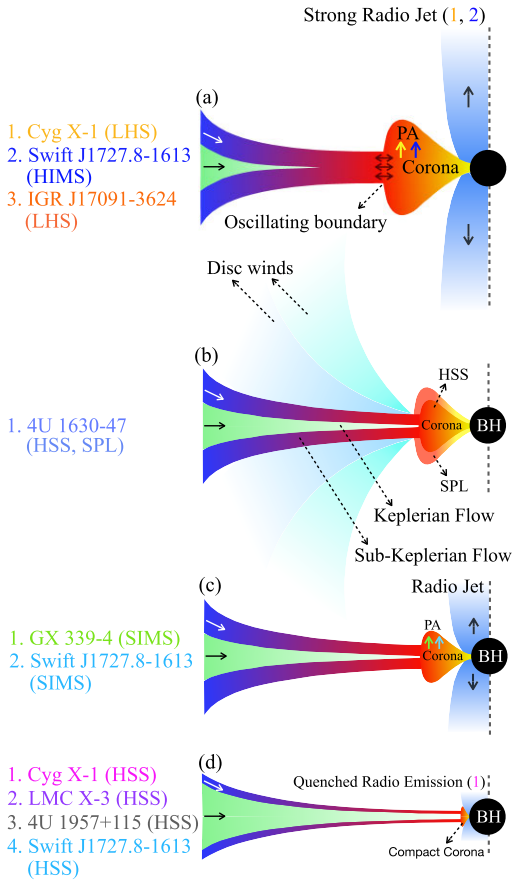

Figure 7. Schematic representation of the possible disc–corona–jet configurations for seven BH-XRB sources within the two-component accretion flow framework. The Keplerian and sub-Keplerian components shown in panel (b) are also present in the other three configurations. Coloured vertical arrows in the corona regions of panels (a) and (c) denote the polarization angle for the respective sources. In panels (a) and (d), the jet/radio emission configuration applies only to sources in distinct spectral states, indicated by their serial numbers. See the text for details.

The spectro-polarimetric correlation study (see Section 4.6 and Fig. 6) suggests that the polarization signatures (PD ∼3 per cent–9 per cent) in the LHS/HIMS of Cyg X−1, *Swift* J1727.8–1613, and IGR J17091–3624 are primarily governed by the dominant Comptonization process characterized by $F_{\rm ratio} < 1$ and $cov_{\rm frac} \sim$ 35 per cent–87 per cent. Interestingly, the radio jet position angle of Cyg X−1 and *Swift* J1727.8–1613 roughly aligns along the observed PA throughout the respective *IXPE* campaigns (J. C. A. Miller-Jones et al. 2021; C. M. Wood et al. 2024). This suggests that PA is possibly oriented perpendicular to the disc-corona geometry. Further, it may be noted that PA resulting from multiple Compton up-scatterings generally tends to align along the minor axis of the corona (A. Ingram et al. 2024). These pieces of evidence suggest a disc–corona configuration comprising a radial corona located close to the black hole, along with a truncated accretion disc at larger radius during LHS/HIMS (see Fig. 7a) of *Swift* J1727.8–1613 and Cyg X−1. The above configuration potentially explains the QPOs in *Swift* J1727.8–1613 (see Section 4.2 and Fig. 2c) in terms of the oscillating boundary of the Comptonizing region (see Fig. 7a and D. Molteni et al. 1996; A. Nandi et al. 2024). It is worth mentioning that the coronal geometry in IGR J17091–3624 remains inconclusive from the polarimetric results due to the unresolved position angle of the radio jet. Although the presence of QPO in LHS of IGR J17091–3624 (see Fig. 2g) perhaps indicates a similar disc–corona configuration presented in Fig. 7(a). However, the absence of QPO in Cyg X−1 implies that either the coronal boundary fails to satisfy the necessary resonance condition for modulation, or oscillation is too subtle to be detected as predicted by S. Majumder, S. Das & A. Nandi (2025).

For 4U 1630–47, an absorption feature around ∼ 7 keV is observed, suggesting the presence of strong disc winds in the HSS ($F_{\rm ratio} \sim 52$ and $cov_{\rm frac} \sim 5$ per cent) spectra (see Section 4.2). Accordingly, a disc-dominated accretion configuration along with a weak corona, accompanied by strong disc winds with varying opening angles (see also A. P. Nitindala et al. 2025), is likely favoured for this source (see Fig. 7b). However, a relatively strong corona ($cov_{\rm frac} \sim 38$ per cent) may be present in the SPL state as compared to the HSS (see Fig. 7b).

For GX 339–4, a low PD (∼ 1.2 per cent) is observed within 3–8 keV energy range during SIMS ($cov_{\rm frac} \sim 34$ per cent and $F_{\rm ratio} \sim 2.4$), while null-detection of PD is seen in the HSS (Table 5). This possibly associates the polarization signature of the source with Comptonized emission. We notice PD $<$ MDP$_{99}$% in the entire *IXPE* energy range of 2–8 keV during SIMS, which possibly resulted from the depolarization of the overall radiation by unpolarized and/or oppositely polarized (as compared to corona) disc emission (A. Ingram et al. 2024) at lower energies (2–3 keV). The polarization angle of GX 339–4 aligns with the direction of the discrete radio jet knot (G. Mastroserio et al. 2025). These findings predict the GX 339–4 configuration comprising a radially extended weak compact corona coexisting with a strong disc ($F_{\rm ratio} \sim 2.4$, $\Gamma_{\rm th} \sim 2$), as illustrated in Fig. 7(c). Moreover, a type-B QPO (see Fig. 2e) observed in this source could be explained from this configuration using an analogous argument presented above for Fig. 7 a (see also A. Nandi et al. 2012; U. Aneesha et al. 2024). Notably, the SIMS of *Swift* J1727.8–1613 also corresponds to the configuration shown in Fig. 7(c).

Furthermore, we conjecture that a similar disc–corona configuration (see Fig. 7d) is also preferred in the disc-dominated HSS of other sources (LMC X−3, 4U 1957 + 115, Cyg X−1, and *Swift* J1727.8–1613) with major contributions from thermal disc and/or various general relativistic effects (L. Marra et al. 2024; J. F. Steiner et al. 2024; S. Majumder et al. 2024a; J. Svoboda et al. 2024a, b) in the observed PD (1.4 per cent–3 per cent). Among these, quenched radio emission with flux densities of $\sim 2.4 - 11.7$ mJy is observed in the HSS of Cyg X−1 (see Table 1 and Fig. 7d), which is found to be consistent with previous reports of radio quenching in this source (S. P. Tigelaar et al. 2004). It is noteworthy that although the presence of a radial corona is favoured for 4U 1630–47, LMC X−3, and 4U 1957 + 115 in Fig. 7, the coronal geometry remains uncertain due to the lack of resolved radio jet orientation for these sources. Moreover, high PD (up to ∼ 21 per cent) dominated by reflected emission in Cyg X−3 appears inconsistent with the disc–corona configurations presented in Fig. 7. It has been suggested that a disc–corona geometry featuring an optically thick funnel in the innermost region of the accretion disc, which obscures most of the primary emission, is favoured for Cyg X−3 (A. Veledina et al. 2024a, b). Finally, we mention that, although the two-component accretion flow configuration aligns with the disc–corona geometry inferred from polarimetric studies for most of the BH-XRBs, a detailed radiative transfer computation is needed within this framework for the predictions on X-ray polarization. Therefore, the schematic in Fig. 7 illustrates a possible disc–corona–jet geometry in BH-XRBs; however, it does not yet provide a quantitative explanation for the polarimetric results.

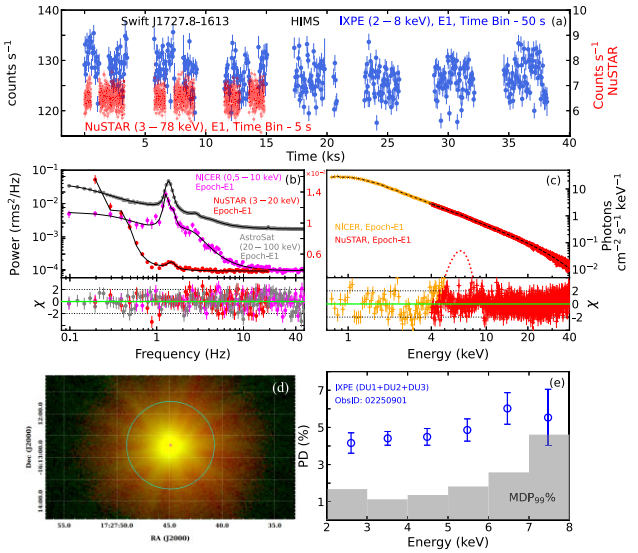

Figure 8. (a) Time binned (50 s) light curve of *Swift* J1727.8–1613 observed with *IXPE* in the hard-intermediate state (HIMS). (b) Best-fitting power density spectra (0.1–50 Hz) obtained from the quasi-simultaneous *NICER* (0.5–10 keV), *NuSTAR* (3–20 keV), and *AstroSat* (20–100 keV) observations. (c) Best-fitting energy spectra from the quasi-simultaneous *NICER* and *NuSTAR* observations in 0.7–40 keV energy range. (d) Colour composite X-ray image (*NuSTAR*: reddish and *IXPE*: greenish) of *Swift* J1727.8 − 1613 with the overlap in yellow colour. The magenta cross marks the source location in X-ray and the cyan circle of radius 60 arcsec around it denotes the region considered for polarimetric analysis. (e) Variation of the polarization degree with energy obtained from the model-independent polarimetric analysis. The grey histograms represent the MDP$_{99}$% level.

5.4 Frontiers of X-ray polarimetry: a promising era ahead

Indeed, the first X-ray polarization measurements were conducted in the 1970s by *OSO-8*, revealing significant polarization in Cyg X−1 with PD $\sim$ 2.4 per cent at 2.6 keV and $\sim$ 5.3 per cent at 5.2 keV (K. S. Long, G. A. Chanan & R. Novick 1980). Thereafter, higher polarization was observed in hard X-rays for Cyg X−1 with *INTEGRAL* as $\lesssim$ 20 per cent in the 130–230 keV band (E. Jourdain et al. 2012) and $\sim$ 75 per cent above 400 keV (J. Rodriguez et al. 2015). Recently, T. Chattopadhyay et al. (2024) detected $\sim$ 23 per cent polarization in the HIMS of Cyg X−1 using *AstroSat*/CZTI. Despite these advances, low-energy X-ray polarimetry remained relatively underexplored until the launch of *IXPE*, which has made substantial progress in this domain during its first three and a half years of operation. Nevertheless, several questions remain unanswered, paving the way for future research.

At present, *Swift* J1727.8–1613 is the only BH-XRB transient observed during its outburst with *IXPE* exhibiting polarization over four spectral states (HIMS, SIMS, HSS, and LHS) along with QPO features. To establish robust spectro-polarimetric correlations across different spectral states, coordinated *IXPE* observations along with simultaneous spectro-temporal coverage from other missions are indispensable. Further, since the effects of Comptonization become prominent beyond the coverage of *IXPE* up to 8 keV, complementary wide-band X-ray spectro-polarimetry and timing studies are crucial to constrain the coronal geometry. Thus, the four windows of X-ray astronomy (imaging, timing, spectroscopy, and polarimetry) with wide energy coverage is crucial to unravel the complete understanding of BH-XRBs (see Fig. 8).

In this context, the recently launched *XPoSat*[10] (X-ray Polarimeter Satellite) mission and the upcoming *XL-Calibur* mission (Q. Abarr et al. 2021) are set to play a crucial role in investigating hard X-ray polarimetric properties of BH-XRBs.In particular, POLIX (Polarimeter Instrument in X-rays) (8–30 keV) and XSPECT (X-ray Spectroscopy and Timing) (0.8–15 keV) onboard *XPoSat* are suitable for mid-energy polarimetry and simultaneous spectro-temporal studies, respectively.The balloon-borne *XL-Calibur* mission, operating in 15–80 keV energy range, completed a successful flight[11] in July 2024, aiming to measure polarization in Cyg X−1. This eventually led to the recent measurement of a polarization degree of $\sim$ 5 per cent in LHS of Cyg X−1 in $\sim$ 19 − 64 keV energy range (H. Awaki et al. 2025), which is comparable to the low energy (2–8 keV) polarimetric results of Cyg X−1 (PD $\sim$ 4.8 per cent, LHS) with *IXPE* (see Fig. 4 and Table 5). The consistency of the measured PDs and PAs across the 2–64 keV range observed with *IXPE* and *XL-Calibur* indicates that the same underlying physical processes likely govern the observed polarization in both energy bands (H. Awaki et al. 2025). In addition, the future soft X-ray spectro-polarimetric mission *eXTP*[12] (2–10 keV), expected to launch in 2027, will offer improved sensitivity for low-energy polarization measurements. Indeed, these dedicated missions will significantly advance our understanding of the accretion dynamics and coronal geometries in BH-XRBs. However, simultaneous observations combining wide-band timing and spectro-polarimetric measurement are still lacking, which emphasizes the need for future missions with broader energy ranges and enhanced capabilities.

6 CONCLUSIONS

In this paper, we perform a detailed timing and spectro-polarimetric study of 11 BH-XRBs using quasi-simultaneous *IXPE*, *NICER*, *NuSTAR,* and *AstroSat* observations. Our analyses provide valuable insights into the accretion-ejection dynamics and the geometry of BH-XRBs under consideration. The key findings from our study along with their implications are summarized below.

(i) The combined spectro-temporal results in the wide-band energy range (0.5–100 keV) reveal the presence of distinct canonical spectral states of BH-XRBs, which are closely connected to the temporal characteristics and emission mechanism of the sources. The timing and spectral features result in degeneracy among the different viable disc-corona geometries of the sources.

(ii) The detection of X-ray polarization is reconfirmed in 8 out of 11 BH-XRBs with moderate to strong energy dependence in PD. A comprehensive spectro-polarimetric correlation study reveals significant positive (negative) correlations between PD and $cov_{\rm frac}$ ($F_{\rm ratio}$) indicating contributions from various surrounding components (disc and corona) to the observed polarization.

(iii) Timing and spectro-polarimetric results, combined with known radio-jet angles, suggest that a two-component disc–corona model may be plausible. In this framework, a radially extended strong corona is likely to be present at the inner part of a truncated accretion disc during harder states, while a comparatively weaker corona persists in softer states for Swift J1727.8−1613, Cyg X−1, GX 339−4, and IGR J17091−3624.

(iv) For 4U 1630−47, LMC X−3, and 4U 1957+115, a thermally dominated accretion disc with a weak corona seems to be preferred.

[10] https://www.isro.gov.in/XPoSat.html
[11] https://sscspace.com/nasa-xl-calibur-balloon-launched/
[12] https://heasarc.gsfc.nasa.gov/docs/heasarc/missions/extp.html

However, the coronal geometry remains unclear due to the minimal contribution of Comptonized emission in the *IXPE* band and the lack of complementary radio observations, though this analysis does support the presence of disc winds in 4U 1630−47. We also note that the disc–corona geometry outlined in this work bears limitations to explain the observed features of Cyg X−3, for which an alternative configuration involving an optically thick inner funnel has been proposed (A. Veledina et al. 2024a, b).

ACKNOWLEDGEMENTS

Authors thank the anonymous reviewer for constructive comments and useful suggestions that helped to improve the quality of the manuscript. SM and SD thank the Department of Physics, IIT Guwahati, India for providing the facilities to complete this work. SM also thanks Luca Baldini for the discussion in identifying the bugs in IXPEOBSSIM software and releasing the latest version IXPEOBSSIM V31.0.3. AK, SS, KJ, and AN thank GH, SAG; DD, PDMSA, and Director, URSC for encouragement and continuous support to carry out this research. This publication uses data from the *IXPE*, *NICER*, *NuSTAR,* and *AstroSat* missions. This research has made use of the *MAXI* data provided by *RIKEN*, *JAXA*, and the *MAXI* team (M. Matsuoka et al. 2009). The *Swift*/BAT transient monitor results provided by the *Swift*/BAT team are also used (H. A. Krimm et al. 2013). We thank each instrument team for processing the data and providing the necessary software tools for the analysis.

DATA AVAILABILITY

Data used for this publication from *IXPE*, *NICER,* and *NuSTAR* missions are currently available at the HEASARC browse (https://heasarc.gsfc.nasa.gov/db-perl/W3Browse/w3browse.pl). The *AstroSat* data are available at the ISSDC data archive (https://webapps.issdc.gov.in/astro_archive/archive/Home.jsp). The *MAXI*/GSC on-demand data are available at http://maxi.riken.jp/mxondem/ and *Swift*/BAT data are taken from https://swift.gsfc.nasa.gov/results/transients/.

REFERENCES

Abarr Q. et al., 2021, Astropart. Phys., 126, 102529
Agrawal P. C., 2006, Adv. Space Res., 38, 2989
Aneesha U., Das S., Katoch T. B., Nandi A., 2024, MNRAS, 532, 4486
Antia H. M. et al., 2017, ApJS, 231, 10
Antia H. M. et al., 2021, JA&A, 42, 32
Antia H. M., Agrawal P. C., Katoch T., Manchanda R. K., Mukerjee K., Shah P., 2022, ApJS, 260, 40
Athulya M. P., Radhika D., Agrawal V. K., Ravishankar B. T., Naik S., Mandal S., Nandi A., 2022, MNRAS, 510, 3019
Awaki H. et al., 2025, ApJ, 994, 37
Baby B. E., Agrawal V. K., Ramadevi M. C., Katoch T., Antia H. M., Mandal S., Nandi A., 2020, MNRAS, 497, 1197
Baldini L. et al., 2022, SoftwareX, 19, 101194
Barillier E., Grinberg V., Horn D., Nowak M. A., Remillard R. A., Steiner J. F., Walton D. J., Wilms J., 2023, ApJ, 944, 165
Bellavita C., García F., Méndez M., Karpouzas K., 2022, MNRAS, 515, 2099
Bellavita C., Méndez M., García F., Ma R., König O., 2025, A&A, 696, A128
Belloni T., Méndez M., van der Klis M., Lewin W. H. G., Dieters S., 1999, ApJ, 519, L159
Belloni T., Psaltis D., van der Klis M., 2002, ApJ, 572, 392
Belloni T., Homan J., Casella P., van der Klis M., Nespoli E., Lewin W. H. G., Miller J. M., Méndez M., 2005, A&A, 440, 207
Beloborodov A. M., 1998, ApJ, 496, L105
Bhuvana G. R., Radhika D., Agrawal V. K., Mandal S., Nandi A., 2021, MNRAS, 501, 5457
Capitanio F., Del Santo M., Bozzo E., Ferrigno C., De Cesare G., Paizis A., 2012, MNRAS, 422, 3130
Casella P., Belloni T., Stella L., 2005, ApJ, 629, 403
Chakrabarti S. K., 1996, ApJ, 464, 664
Chakrabarti S. K., Manickam S. G., 2000, ApJ, 531, L41
Chakrabarti S., Titarchuk L. G., 1995, ApJ, 455, 623
Chakrabarti S. K., Debnath D., Nandi A., Pal P. S., 2008, A&A, 489, L41
Chandrasekhar S., 1960, Radiative Transfer. Dover Publications, New York
Chatterjee K., Debnath D., Bhowmick R., Nath S. K., Chatterjee D., 2022, MNRAS, 510, 1128
Chatterjee K., Pujitha Suribhatla S., Mondal S., Singh C. B., 2024, ApJ, 987, 44
Chattopadhyay T. et al., 2024, ApJ, 960, L2
Contopoulos G., Jappel A., 1974, in Trans. IAU Vol._XVB: Proc. 15th General Assembly, Sydney 1973 and Extraordinary Assembly. D. Reidel, Dordrecht, p. 334
Das S., Chattopadhyay I., Nandi A., Molteni D., 2014, MNRAS, 442, 251
Dauser T., Garcia J., Wilms J., Böck M., Brenneman L. W., Falanga M., Fukumura K., Reynolds C. S., 2013, MNRAS, 430, 1694
Debnath D., Srimani S., Chang H.-K., 2025, ApJ, 989, 165
Dexter J., Begelman M. C., 2024, MNRAS, 528, L157
Done C., Zycki P. T., 1999, MNRAS, 305, 457
Done C., Gierliński M., Kubota A., 2007, A&AR, 15, 1
Dovčiak M. et al., 2024, Galaxies, 12, 54
Eardley D. M., Lightman A. P., Shapiro S. L., 1975, ApJ, 199, L153
Ewing M. et al., 2025, MNRAS, 541, 1774
Fender R. P., Homan J., Belloni T. M., 2009, MNRAS, 396, 1370
García F., Méndez M., Karpouzas K., Belloni T., Zhang L., Altamirano D., 2021, MNRAS, 501, 3173
García J. et al., 2014, ApJ, 782, 76
Garg A., Rawat D., Méndez M., 2024, MNRAS, 531, 585
Gendreau K. C. et al., 2016, in den Herder J.-W. A., Takahashi T., Bautz M., eds, Proc. SPIE Conf. Ser. Vol. 9905, Space Telescopes and Instrumentation 2016: Ultraviolet to Gamma Ray. SPIE, Bellingham, p. 99051H
Giacconi R., Gorenstein P., Gursky H., Waters J. R., 1967, ApJ, 148, L119
Giacconi R., Murray S., Gursky H., Kellogg E., Schreier E., Matilsky T., Koch D., Tananbaum H., 1974, ApJS, 27, 37
Gomez S., Mason P. A., Robinson E. L., 2015, ApJ, 809, 9
Gou L. et al., 2009, ApJ, 701, 1076
Gou L. et al., 2014, ApJ, 790, 29
Haardt F., Maraschi L., 1993, ApJ, 413, 507
Harrison F. A. et al., 2013, ApJ, 770, 103
Homan J., Wijnands R., van der Klis M., Belloni T., van Paradijs J., Klein-Wolt M., Fender R., Méndez M., 2001, ApJS, 132, 377
Homan J. et al., 2020, ApJ, 891, L29
Ingram A. R., Motta S. E., 2019, New Astron. Rev., 85, 101524
Ingram A., Done C., Fragile P. C., 2009, MNRAS, 397, L101
Ingram A. et al., 2024, ApJ, 968, 76
Iyer N., Nandi A., Mandal S., 2015, ApJ, 807, 108
Jana A., Chang H.-K., 2024, MNRAS, 527, 10837
Jones C., Forman W., Tananbaum H., Turner M. J. L., 1976, ApJ, 210, L9
Jourdain E., Roques J. P., Chauvin M., Clark D. J., 2012, ApJ, 761, 27
Kalemci E., Maccarone T. J., Tomsick J. A., 2018, ApJ, 859, 88
Karpouzas K., Méndez M., Ribeiro E. M., Altamirano D., Blaes O., García F., 2020, MNRAS, 492, 1399
Katoch T., Baby B. E., Nandi A., Agrawal V. K., Antia H. M., Mukerjee K., 2021, MNRAS, 501, 6123
Kennea J. A., Lien A. Y., D'Elia V., Melandri A., Page K. L., Siegel M. H., 2024, Astron. Telegram, 16500, 1
Kislat F., Clark B., Beilicke M., Krawczynski H., 2015, Astropart. Phys., 68, 45
Krawczynski H. et al., 2022, Science, 378, 650
Krawczynski H. et al., 2024, ApJ, 977, L10
Krimm H. A. et al., 2013, ApJS, 209, 14
Kudo Y. et al., 2025, Astron. Telegram, 16975, 1
Kumar N., 2024, PASA, 41, e013
Kushwaha A., Agrawal V. K., Nandi A., 2021, MNRAS, 507, 2602

Kushwaha A., Jayasurya K. M., Agrawal V. K., Nandi A., 2023, MNRAS, 524, L15
Kuulkers E., Lutovinov A., Parmar A., Capitanio F., Mowlavi N., Hermsen W., 2003, Astron. Telegram, 149, 1
Kylafis N. D., Reig P., Papadakis I., 2020, A&A, 640, L16
Liao J. et al., 2024, ApJ, 986, 3
Ling Y.-S., Xie F., Ge M.-Y., Monaca F. L., 2024, Res. Astron. Astrophys., 24, 095004
Liu H. X. et al., 2022, ApJ, 938, 108
Long K. S., Chanan G. A., Novick R., 1980, ApJ, 238, 710
Ma X. et al., 2021, Nat. Astron., 5, 94
Maitra D., Miller J. M., Reynolds M. T., Reis R., Nowak M., 2014, ApJ, 794, 85
Majumder P., Dutta B. G., Nandi A., 2025, MNRAS, 540, 37
Majumder S., Sreehari H., Aftab N., Katoch T., Das S., Nandi A., 2022, MNRAS, 512, 2508
Majumder S., Kushwaha A., Das S., Nandi A., 2024a, MNRAS, 527, L76
Majumder S., Chatterjee R., Jayasurya K. M., Das S., Nandi A., 2024b, ApJ, 971, L21
Majumder S., Das S., Nandi A., 2025, MNRAS, 539, 2064
Makishima K., Maejima Y., Mitsuda K., Bradt H. V., Remillard R. A., Tuohy I. R., Hoshi R., Nakagawa M., 1986, ApJ, 308, 635
Mandel S. et al., 2025, Astron. Telegram, 17031, 1
Mark H., Price R., Rodrigues R., Seward F. D., Swift C. D., 1969, ApJ, 155, L143
Markert T. H., Canizares C. R., Clark G. W., Lewin W. H. G., Schnopper H. W., Sprott G. F., 1973, ApJ, 184, L67
Markoff S., Nowak M. A., Wilms J., 2005, ApJ, 635, 1203
Marra L. et al., 2024, A&A, 684, A95
Marra L. et al., 2025, preprint (arXiv:2506.17050)
Mastroserio G. et al., 2025, ApJ, 978, L19
Mata Sánchez D., Muñoz-Darias T., Armas Padilla M., Casares J., Torres M. A. P., 2024, A&A, 682, L1
Matsuoka M. et al., 2009, PASJ, 61, 999
McClintock J. E., Remillard R. A., Rupen M. P., Torres M. A. P., Steeghs D., Levine A. M., Orosz J. A., 2009, ApJ, 698, 1398
Méndez M., Karpouzas K., García F., Zhang L., Zhang Y., Belloni T. M., Altamirano D., 2022, Nat. Astron., 6, 577
Miller-Jones J. C. A. et al., 2021, Science, 371, 1046
Miyamoto S., Kitamoto S., 1991, ApJ, 374, 741
Molteni D., Sponholz H., Chakrabarti S. K., 1996, ApJ, 457, 805
Mondal S., Suribhatla S. P., Chatterjee K., Singh C. B., Chatterjee R., 2024, ApJ, 975, 257
Morgan E. H., Remillard R. A., Greiner J., 1997, ApJ, 482, 993
Nakajima M. et al., 2023, Astron. Telegram, 16206, 1
Nandi A., Debnath D., Mandal S., Chakrabarti S. K., 2012, A&A, 542, A56
Nandi A., Das S., Majumder S., Katoch T., Antia H. M., Shah P., 2024, MNRAS, 531, 1149
Nitindala A. P., Veledina A., Poutanen J., 2025, A&A, 694, A230
Orosz J. A. et al., 2009, ApJ, 697, 573
Orosz J. A., Steiner J. F., McClintock J. E., Buxton M. M., Bailyn C. D., Steeghs D., Guberman A., Torres M. A. P., 2014, ApJ, 794, 154
Pahari M. et al., 2018, ApJ, 867, 86
Parker M. L. et al., 2016, ApJ, 821, L6
Parmar A. N., Angelini L., White N. E., 1995, ApJ, 452, L129
Peng J.-Q. et al., 2024a, ApJ, 960, L17
Peng J.-Q. et al., 2024b, ApJ, 973, L7
Peters W. M., Polisensky E., Clarke T. E., Giacintucci S., Kassim N. E., 2023, Astron. Telegram, 16279, 1
Pietrzyński G. et al., 2013, Nature, 495, 76
Podgorný J. et al., 2023, MNRAS, 526, 5964
Podgorný J. et al., 2024, A&A, 686, L12
Poutanen J., Krolik J. H., Ryde F., 1997, MNRAS, 292, L21
Poutanen J., Veledina A., Beloborodov A. M., 2023, ApJ, 949, L10
Prabhakar G., Mandal S., Bhuvana G. R., Nandi A., 2023, MNRAS, 520, 4889
Radhika D., Nandi A., 2014, Adv. Space Res., 54, 1678
Radhika D., Nandi A., Agrawal V. K., Seetha S., 2016, MNRAS, 460, 4403
Radhika D., Sreehari H., Nandi A., Iyer N., Mandal S., 2018, Ap&SS, 363, 189
Ratheesh A. et al., 2024, ApJ, 964, 77
Rawat D., Garg A., Méndez M., 2023a, MNRAS, 525, 661
Rawat D., Garg A., Méndez M., 2023b, ApJ, 949, L43
Reid M. J., Miller-Jones J. C. A., 2023, ApJ, 959, 85
Remillard R. A., McClintock J. E., 2006, ARA&A, 44, 49
Remillard R. A. et al., 2022, AJ, 163, 130
Rodriguez Cavero N. et al., 2023, ApJ, 958, L8
Rodriguez J., Corbel S., Caballero I., Tomsick J. A., Tzioumis T., Paizis A., Cadolle Bel M., Kuulkers E., 2011, A&A, 533, L4
Rodriguez J. et al., 2015, ApJ, 807, 17
Schnittman J. D., Krolik J. H., 2009, ApJ, 701, 1175
Seifina E., Titarchuk L., Shaposhnikov N., 2014, ApJ, 789, 57
Shakura N. I., Sunyaev R. A., 1973, A&A, 24, 337
Shui Q.-C. et al., 2024, ApJ, 973, 59
Smale A. P., Boyd P. T., 2012, ApJ, 756, 146
Soleri P., Belloni T., Casella P., 2008, MNRAS, 383, 1089
Sreehari H., Iyer N., Radhika D., Nandi A., Mandal S., 2019a, Adv. Space Res., 63, 1374
Sreehari H., Ravishankar B. T., Iyer N., Agrawal V. K., Katoch T. B., Mandal S., Nand i A., 2019b, MNRAS, 487, 928
Sreehari H., Nandi A., Das S., Agrawal V. K., Mandal S., Ramadevi M. C., Katoch T., 2020, MNRAS, 499, 5891
Steiner J. F., McClintock J. E., Remillard R. A., Gou L., Yamada S., Narayan R., 2010, ApJ, 718, L117
Steiner J. F. et al., 2024, ApJ, 969, L30
Stella L., Vietri M., 1998, ApJ, 492, L59
Stern B. E., Poutanen J., Svensson R., Sikora M., Begelman M. C., 1995, ApJ, 449, L13
Strohmayer T. E., 2017, ApJ, 838, 72
Svoboda J. et al., 2024a, ApJ, 960, 3
Svoboda J. et al., 2024b, ApJ, 966, L35
Tigelaar S. P., Fender R. P., Tilanus R. P. J., Gallo E., Pooley G. G., 2004, MNRAS, 352, 1015
Titarchuk L., 1994, ApJ, 434, 570
Tomaru R., Done C., Odaka H., 2024, MNRAS, 527, 7047
Tomsick J. A., Lapshov I., Kaaret P., 1998, ApJ, 494, 747
Tomsick J. A. et al., 2013, ApJ, 780, 78
Torpin T. J., Boyd P. T., Smale A. P., Valencic L. A., 2017, ApJ, 849, 32
van Kerkwijk M. H. et al., 1992, Nature, 355, 703
Veledina A. et al., 2023, ApJ, 958, L16
Veledina A. et al., 2024a, Nat. Astron., 8, 1031
Veledina A. et al., 2024b, A&A, 688, L27
Wang J. et al., 2024, ApJ, 963, 14
Wang Y., Méndez M., Altamirano D., Court J., Beri A., Cheng Z., 2018, MNRAS, 478, 4837
Webster B. L., Murdin P., 1972, Nature, 235, 37
Weisskopf M. C. et al., 2022, J. Astron. Telesc. Instrum. Syst., 8, 026002
Williams-Baldwin D., Motta S., Rhodes L., Carotenuto F., Fender R., Beswick R., 2023, Astron. Telegram, 16231, 1
Wilms J., Allen A., McCray R., 2000, ApJ, 542, 914
Wood C. M. et al., 2024, ApJ, 971, L9
Xu Y. et al., 2017, ApJ, 851, 103
Zdziarski A. A., Johnson W. N., Magdziarz P., 1996, MNRAS, 283, 193
Zdziarski A. A., Szanecki M., Poutanen J., Gierliński M., Biernacki P., 2020, MNRAS, 492, 5234
Zdziarski A. A., Banerjee S., Szanecki M., Misra R., Dewangan G., 2024, ApJ, 981, L15
Zhang Y. et al., 2023, MNRAS, 520, 5144
Zhao X. et al., 2021, ApJ, 908, 117

This paper has been typeset from a TEX/LATEX file prepared by the author.